Monthly Notices of the ROYAL ASTRONOMICAL SOCIETY

MNRAS **538,** 198–222 (2025) https://doi.org/10.1093/mnras/staf278
Advance Access publication 2025 February 19

PAMS: The Perseus Arm Molecular Survey–I. Survey description and first results

Andrew J. Rigby [1]★ Mark A. Thompson,[1] David J. Eden [2,3] Toby J. T. Moore,[4] Mubela Mutale,[1] Nicolas Peretto [5] Rene Plume,[6] James S. Urquhart [7] Gwenllian M. Williams [8] and Malcolm J. Currie[9]

[1]*School of Physics and Astronomy, University of Leeds, Leeds LS2 9JT, UK*
[2]*Physics Department, University of Bath, Claverton Down, Bath BA2 7AY, UK*
[3]*Armagh Observatory and Planetarium, College Hill, Armagh BT61 9DB, UK*
[4]*Astrophysics Research Institute, Liverpool John Moores University, Liverpool Science Park, 146 Brownlow Hill, Liverpool L3 5RF, UK*
[5]*Cardiff Hub for Astrophysics Research and Technology, School of Physics and Astronomy, Cardiff University, Queens Buildings, Cardiff CF24 3AA, UK*
[6]*Department of Physics and Astronomy, University of Calgary, 2500 University Drive NW, Calgary, Alberta T2N 1N4, Canada*
[7]*Centre for Astrophysics and Planetary Science, University of Kent, Canterbury CT2 7NH, UK*
[8]*Department of Physics, Aberystwyth University, Penglais, Aberystwyth, Ceredigion SY23 3BZ, UK*
[9]*RAL Space, STFC Rutherford Appleton Laboratory, Didcot OX11 0QX, UK*

Accepted 2025 February 10. Received 2025 January 20; in original form 2024 June 14

ABSTRACT

The external environments surrounding molecular clouds vary widely across galaxies such as the Milky Way, and statistical samples of clouds are required to understand them. We present the Perseus Arm Molecular Survey (PAMS), a James Clerk Maxwell Telescope (JCMT) survey combining new and archival data of molecular-cloud complexes in the outer Perseus spiral arm in ^{12}CO, ^{13}CO, and C^{18}O ($J = 3$–2). With a survey area of ∼8 deg^2, PAMS covers well-known complexes such as W3, W5, and NGC 7538 with two fields at $\ell \approx 110^\circ$ and $\ell \approx 135^\circ$. PAMS has an effective resolution of 17 arcsec, and rms sensitivity of $T_{\rm mb} = 0.7$–1.0 K in 0.3 km s^{-1} channels. Here we present a first look at the data, and compare the PAMS regions in the Outer Galaxy with Inner Galaxy regions from the CO Heterodyne Inner Milky Way Plane Survey (CHIMPS). By comparing the various CO data with maps of H_2 column density from *Herschel*, we calculate representative values for the CO-to-H_2 column-density X-factors, which are $X_{^{12}{\rm CO}\,(3-2)} = 4.0 \times 10^{20}$ and $X_{^{13}{\rm CO}\,(3-2)} = 4.0 \times 10^{21}$ cm^{-2} (K km s^{-1})$^{-1}$ with a factor of 1.5 uncertainty. We find that the emission profiles, size–linewidth, and mass–radius relationships of ^{13}CO-traced structures are similar between the Inner and Outer Galaxy. Although PAMS sources are slightly more massive than their Inner Galaxy counterparts for a given size scale, the discrepancy can be accounted for by the Galactic gradient in gas-to-dust mass ratio, uncertainties in the X-factors, and selection biases. We have made the PAMS data publicly available, complementing other CO surveys targeting different regions of the Galaxy in different isotopologues and transitions.

Key words: molecular data – surveys – stars: formation – ISM: clouds – galaxies: ISM – submillimetre: ISM.

1 INTRODUCTION

Star clusters form within regions of giant molecular clouds (GMCs) where self-gravity is able to overcome opposing physical processes such as thermal pressure, turbulence, and magnetic fields. There are many properties within the interstellar medium (ISM) of a galaxy that vary from one location to another, and these environmental differences could reasonably be expected to leave an imprint upon the process of star formation. For example, in the Milky Way, there are several key differences between the Inner and Outer Galaxy, which we define here as the regions inside and outside of the Sun's orbit with a Galactocentric radius of $R_{\rm GC} = 8.15 \pm 0.15$ kpc (Reid et al. 2019), respectively. The molecular-to-atomic gas ratio, drops from a value of $f_{\rm mol} \approx 1$ in the central molecular zone (CMZ, $R_{\rm GC} < 0.5$ kpc) at the centre of the Galaxy, to $f_{\rm mol} \approx 0.1$ at $R_{\rm GC} = 10$ kpc (Sofue & Nakanishi 2016). The strength of the interstellar radiation field (Popescu et al. 2017), dust temperature (Marsh et al. 2017), metallicity (Luck & Lambert 2011), and the ratio of solenoidal to compressive turbulence within molecular clouds (Rani et al. 2022) all decrease with $R_{\rm GC}$.

The CMZ is a significantly different star-forming environment from the Galactic disc, with a star-formation rate (SFR) an order of magnitude lower than would be expected for the same surface density of molecular gas across a galactic disc (e.g. Longmore et al. 2013; Barnes et al. 2017). The low star-formation efficiency (SFE) in the CMZ is accompanied by very large line-of-sight velocity dispersions, and a size–linewidth relationship that is steeper than typically found

★ E-mail: a.j.rigby@leeds.ac.uk

in the Galactic disc (Kauffmann et al. 2017). These results are generally interpreted as signatures of elevated levels of turbulence that suppress the SFR. Federrath et al. (2016) found that turbulent motions within the CMZ cloud G0.253+0.016 are consistent with being dominated by solenoidal modes, which are expected to inhibit star formation (and, conversely, turbulence that is dominated by compressive modes are expected to promote star formation). The authors speculate that shear is responsible for the strong solenoidal modes in the CMZ, caused by the differential rotation of gas that is stronger towards the centres of galaxies.

It may then be expected that as shear decreases, moving from the interior to the exterior of the Galaxy, that solenoidal modes of turbulence become less important. Indeed, Rani et al. (2022) report a negative gradient in the ratio of power in solenoidal to compressive turbulence with Galactocentric radius ($R_{\rm GC}$) for molecular clouds from CHIMPS (Rigby et al. 2016). They found that this is also accompanied by a rise in SFE, indicating that the mode of turbulence may play a role in determining SFE across the Galaxy. While the molecular clouds within the CHIMPS survey cover a relatively wide range of $R_{\rm GC}$, from 4–12 kpc, the number of sources beyond $R_{\rm GC} >$ 8 kpc is relatively small, and the spatial resolution is rather limited due to the large heliocentric distances of $d > 12$ kpc that result from the survey field covering a limited range of low Galactic longitudes (roughly 28° to 46°).

The Outer Galaxy presents a different star-forming environment from the Inner Galaxy and the CMZ. In addition to the various gradients mentioned above that produce different conditions in the Outer Galaxy, dynamical features also differ in important ways. The interval between the passage of spiral arms is relatively long, and the spiral arms themselves are wider (Reid et al. 2019). The spiral structure itself is less regular, with large deviations from logarithmic spirals. The corotation radius is located at $R_{\rm GC}$ ∼7 kpc, outside of which the spiral arm pattern speed exceeds the circular velocity of the gas and stars, and the outer Lindblad resonance is located at $R_{\rm GC}$ ∼11 kpc (Clarke & Gerhard 2022). Although spiral arms do not appear to substantially alter star formation in the Inner Galaxy (e.g. Moore et al. 2012; Eden et al. 2013, 2015; Urquhart et al. 2021; Colombo et al. 2022; Querejeta et al. 2024), these dynamical effects may still have an impact (perhaps indirectly) upon the star-formation process in the Outer Galaxy, where the surface density of molecular clouds and their complexes is much lower.

Large-scale and unbiased surveys of dust continuum – such as The Apex Telescope Large Area Survey of the Galaxy (ATLASGAL; Schuller et al. 2009), and the *Herschel* infrared Galactic Plane Survey (Hi-GAL; Molinari et al. 2016) – and CO–such as the ^{13}CO (1–0) Galactic Ring Survey (GRS; Jackson et al. 2006), CHIMPS (Rigby et al. 2016) in ^{13}CO (3–2), the CO High-Resolution Survey (COHRS; Dempsey, Thomas & Currie 2013; Park et al. 2023) in ^{12}CO (3–2), and the Structure, Excitation, and Dynamics of the Inner Galactic Interstellar Medium (SEDIGISM; Schuller et al. 2017) survey in ^{13}CO (2–1) – have advanced our understating of many of the Galaxy-scale phenomena listed above in the Inner Galaxy.

However, the relative sparsity of sources in the Outer Galaxy (i.e. the number of molecular clouds per unit angular area) mean that it is more difficult to justify the expenditure of time on unbiased (i.e. blind) mapping in molecules rarer than ^{12}CO at moderate resolution. Survey data do exist in the Outer Galaxy: the FCRAO and Exeter-FCRAO CO Galactic Plane Surveys cover $55 \geq \ell \leq 195$ in ^{12}CO and ^{13}CO (1–0) with varying coverage in Galactic latitude at 46-arcsec resolution (Heyer et al. 1998; Wienen et al. 2022, Brunt et al., in preparation); the Forgotten Quadrant survey covers longitudes of $220 < \ell < 240°$ with $2.5 < b < 0.0°$ (Benedettini et al. 2020); and the Milky Way Imaging Scroll Painting survey (MWISP; Su et al. 2019) covers this region within its staggering $-10° \leq \ell \leq 250°$ and $|b| < 5.^{\circ}2$ footprint in ^{12}CO, ^{13}CO, and C^{18}O (1–0) at 50-arcsec resolution. The latest generation of surveys at $\lesssim$ 30-arcsec resolution is only now catching up with their Inner Galaxy counterparts: the FOREST unbiased Galactic Plane imaging survey with the Nobeyama 45-m telescope (FUGIN; Umemoto et al. 2017), covers ^{12}CO, ^{13}CO, and C^{18}O (1–0) at ∼20-arcsec resolution covers $198° \geq \ell \leq 236°$ in the third quadrant, which is now also partially ($215° \geq \ell \leq 225°$) covered by the CHIMPS2 survey (Eden et al. 2020). The CO Large Outer-Galaxy Survey (CLOGS; Eden et al., in preparation) is now extending an area adjoining the CHIMPS2 Outer Galaxy survey, primarily in ^{12}CO, but with follow-ups of bright sources in ^{13}CO and C^{18}O(3–2); and the Outer Galaxy High-Resolution Survey (OGHReS; Urquhart et al. 2024) is also mapping a large area of the third quadrant in the ^{12}CO and ^{13}CO (2–1) with a similar specification as SEDIGISM. In dust continuum, the SCUBA-2 Ambitious Sky Survey (SASSy; Nettke et al. 2017; Thompson et al., in preparation) and SASSy-Perseus (Thompson et al., in preparation) surveys cover $120° < \ell < 250°$ and $60° < \ell < 120°$, respectively, and have been able to map a very large area in 850 μm with a sensitivity comparable to that of ATLASGAL.

The second Galactic quadrant ($90° \leq \ell \leq 180°$) is relatively unexplored at high angular resolution. In this paper we present the 17-arcsec-resolution Perseus Arm Molecular Survey (PAMS), a survey of several Outer Galaxy star-forming regions in the second quadrant in the 3–2 rotational transition of ^{13}CO and C^{18}O, and incorporating new and archival ^{12}CO data that cover most of the PAMS regions. The observations are highly complementary to other CO surveys such as CHIMPS/2, COHRS, and CLOGS, and greatly bolster the available statistics of Outer Galaxy star-forming regions. The surveyed regions include some of the most famous star-forming regions within the Perseus arm in the Outer Galaxy, such as W3, W5, and NGC 7538, which lie at $R_{\rm GC} \approx 9.5$ kpc.

In Section 2 we describe the observations, and we present the data in Section 3. In Section 4 we compare analyses of the CO-to-molecular-hydrogen column-density conversion factor, and basic molecular-cloud scaling relationships between the Outer Galaxy PAMS data and representative Inner Galaxy data from the CHIMPS survey. We discuss our findings and conclusions in Section 6.

2 OBSERVATIONS AND DATA REDUCTION

The data presented here as PAMS are comprised of data cubes of the (3–2) transition of ^{12}CO, ^{13}CO, and C^{18}O for nine regions in the Outer Perseus spiral arm. Eight of those regions were originally targeted for PAMS in ^{13}CO and C^{18}O with observing campaigns in 2009–10, and we have supplemented these with archival ^{12}CO data, where available, and obtained new observations of G110 and S152. By incorporating further archival observations of W3, PAMS covers a total of nine regions, with almost complete coverage in the three isotopologues. The observations and data reduction are detailed below.

2.1 ^{13}CO and C^{18}O (3–2) observations

We conducted simultaneous basket-woven raster mapping observations of ^{13}CO and C^{18}O ($J = 3$–2) at 330.588 and 329.331 GHz using the Heterodyne Array Receiver Programme and Auto-Correlation Spectral Imaging System (HARP/ACSIS; Buckle et al. 2009) at

Table 1. Details of the target regions, in reverse order of Galactic longitude: approximate field centres in Galactic coordinates, representative systemic velocity determined from a Gaussian fit to the mean ^{13}CO (3–2) spectrum, heliocentric distance and uncertainty, Galactocentric distance, total area of the PAMS observations, and the rms values of the various observations on the $T_{\rm mb}$ scale at the two different velocity resolutions.

Region	ℓ	b	$v_{\rm LSR}$	d	Δd	$R_{\rm GC}$	Area	rms ($T_{\rm mb}$) ^{12}CO		^{13}CO		C^{18}O	
								0.3 km s^{-1}	0.5 km s^{-1}	0.3 km s^{-1}	0.5 km s^{-1}	0.3 km s^{-1}	0.5 km s^{-1}
	(°)	(°)	(km s^{-1})	(kpc)	(kpc)	(kpc)	(deg^2)	(K)	(K)	(K)	(K)	(K)	(K)
W5	137.8	1.3	−38.6	1.96	0.04	9.69	2.42	1.01	0.75	0.66	0.51	0.83	0.69
IRAS 02327	135.5	0.3	−43.1	1.96	0.04	9.65	0.03	–	0.91	0.54	0.42	0.72	0.56
G135.2+1.1	135.2	1.1	−44.8	1.96	0.04	9.64	0.14	–	0.60	0.81	0.63	1.05	0.79
G134.9+1.4	134.8	1.4	−40.6	1.96	0.04	9.63	0.06	–	–	0.90	0.70	1.15	0.97
W3	133.5	0.7	−45.4	1.96	0.04	9.60	1.97	0.76	0.59	0.61	0.47	0.84	0.65
NGC 7538	111.6	0.7	−53.1	2.69	0.13	9.48	0.99	–	0.35	0.68	0.53	0.89	0.73
S157	111.3	−0.8	−43.4	3.38	0.15	9.89	0.26	–	0.85	0.97	0.75	1.3	1.0
G110.5−0.5	110.4	−0.3	−51.3	2.72	0.19	9.45	1.57	1.39	1.16	0.67	0.52	0.86	0.7
S147/152	108.8	−1.0	−50.8	2.81	0.22	9.44	0.80	1.00	0.84	0.81	0.63	1.03	0.83
Total							8.24	1.00	0.72	0.68	0.53	0.88	0.71

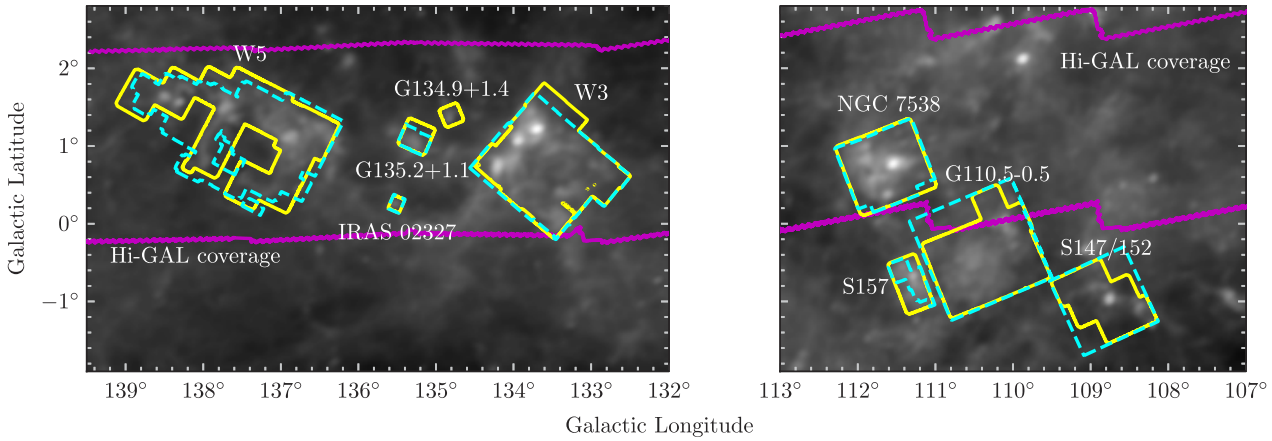

Figure 1. Illustration of the extent of each PAMS region overlaid on *Planck* 857 GHz continuum imaging (Planck Collaboration VI 2020), which is displayed on a logarithmic intensity scale. *Left panel*: the $\ell = 137°$ region. *Right panel*: the $\ell = 111°$ region. The solid and dashed lines show the extent of the PAMS ^{13}CO and C^{18}O(3–2) data, and ^{12}CO (3–2) data, respectively. The extent of Hi-GAL coverage is indicated by the zig-zagged lines.

the 15-m James Clerk Maxwell Telescope (JCMT) on Mauna Kea, Hawaii. The observations, taken in 2009–10, consist of a series of tiles of up to 1020×1020 arcsec in size as part of projects M09BU04 and M10BU08. The targets are listed in Table 1, and the field extents are illustrated upon *Planck* 857 GHz continuum maps (Planck Collaboration VI 2020) in Fig. 1. For each tile, these observations took the form of two sets of position-switched scans at right angles to each other with a quarter array (29.1 arcsec) shift between each scan in a given direction. The same reference positions were used for each tile in a given region, which were checked to ensure they were free of contamination. The 250-MHz bandwidth correlator setting was used with 4096 channels, resulting in a native spectral resolution of ∼0.06 km s^{-1}. The native angular resolution of the JCMT at 330 GHz is 15 arcsec.

Following standard practice at JCMT, pointing was checked between observations, for which the uncertainty is estimated to be 2 arcsec in both azimuth and elevation, resulting in a 3 arcsec radial uncertainty. Calibration was performed using the three-load chopper-wheel method (Kutner & Ulich 1981) during the observations, with which the intensity of the spectra are placed on the corrected antenna temperature (T_A^*) scale. Spectral standards are also monitored throughout observations, and peak and integrated flux densities are generally found to be accurate to within 10 per cent.

2.2 ^{12}CO (3–2) observations

New observations of ^{12}CO (3–2) at 345.796 GHz for the G110 and S152 regions were obtained in the summer of 2024 through programmes M23BN003 (PI: Parsons) and S24BP004 (PI: Eden). The setup was similar to the ^{13}CO and C^{18}O observations except for the following differences: the backend (ACSIS) was configured to use 8192 250-MHz-wide channels, all individual tiles were 1320×1320 arcsec in size, and half-array (58.2 arcsec) spacing was used between rows. The native angular resolution of JCMT at 345 GHz is 14 arcsec.

2.3 Archival observations

We have incorporated further ^{12}CO ($J = 3$–2) data from the JCMT archives covering five of the regions: G135.2+1.1, IRAS 02327, S157, NGC 7538, and W5 have almost complete coverage and, while G110 and S152 had partial coverage in the archive, those data were superseded by our new observations. G134.9+1.4 is the only region that has no ^{12}CO (3–2) coverage. The archival data used were M07AU08 (PI: S. Lumsden), M07BH45B, M08BH15, and M09BC12 (PI: J. Williams), M09BN07 (PI: M. Hogerheijde), M09BH09C (PI: J. Di Francesco) and M10BC04 (PI: M. Reid). The

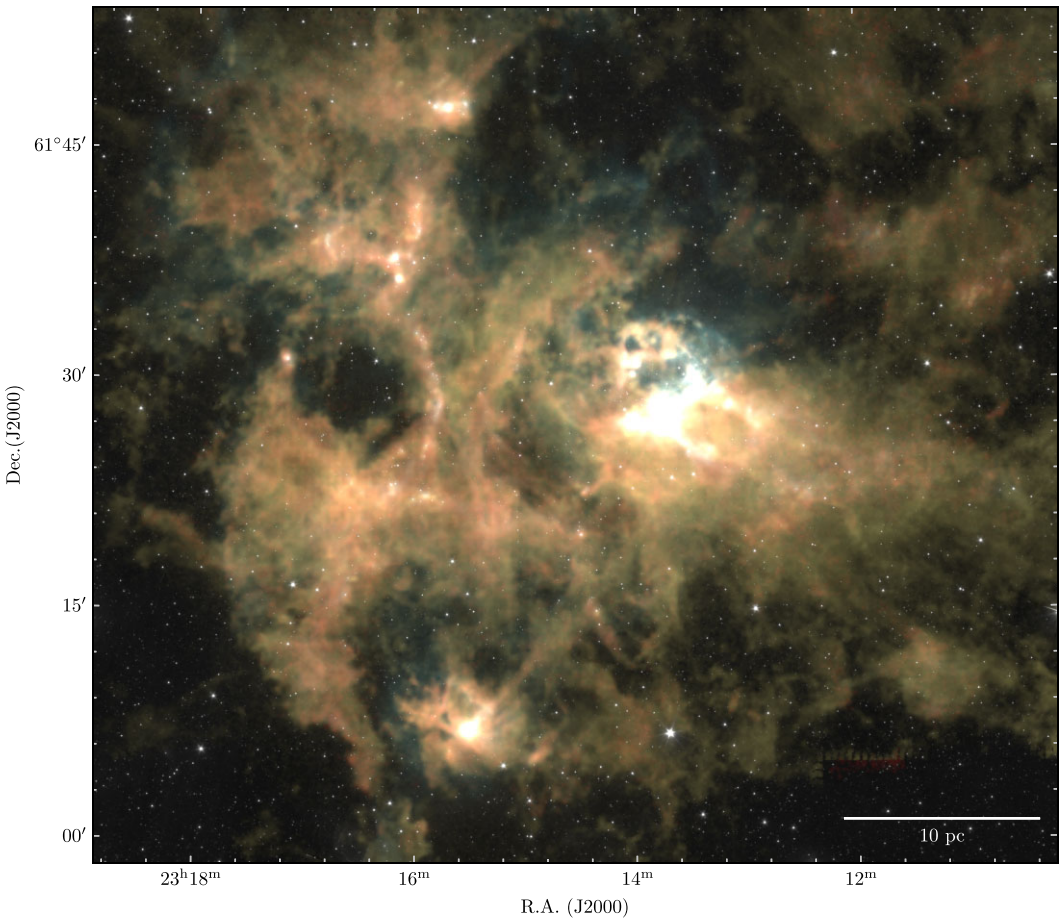

Figure 2. Four colour composite image of NGC 7538. *Spitzer*/GLIMPSE 4.5 μm (Benjamin et al. 2003), *Herschel*/HOBYS 70 μm (Motte et al. 2010), archival JCMT ^{12}CO (3–2) integrated intensity, and JCMT/PAMS ^{13}CO (3–2) integrated intensity images are shown in white, cyan, yellow, and red channels, respectively. The integrated intensity CO and ^{13}CO (3–2) images have been masked as described in Section 3.3, and are individually displayed in Fig. 5.

NGC 7538 and W5 data were previously published in Fallscheer et al. (2013) and Ginsburg, Bally & Williams (2011), respectively, while outflows within G110, S152, and S157 formed part of the sample of Maud et al. (2015).

Additional ^{12}CO, ^{13}CO, and C^{18}O (3–2) observations of the W3 complex were incorporated from observing programmes M06BU21, M07BH17B, M08BU24 (PI: Moore). The W3 data were originally presented in Polychroni, Moore & Allsopp (2012). Some of these observations date from earlier in the lifetime of the then recently commissioned HARP instrument and have a slightly different observing format, most notably that the scans are not all basket-woven.

2.4 Data reduction

Data reduction was performed using ORAC-DR (Jenness et al. 2015), which is built on the Starlink (Currie et al. 2014) packages KAPPA (Currie & Berry 2013), CUPID (Berry et al. 2007), and SMURF (Chapin et al. 2013), with which we used the `REDUCE_SCIENCE_NARROWLINE` recipe. We give the template reduction parameters in Appendix A. The ^{13}CO and C^{18}O data were regridded onto the 6-arcsec pixels using an 8-arcsec full width at half-maximum (FWHM) Gaussian smooth, meaning that the reduced data cubes have an effective angular resolution of 17.2 arcsec. In the vast majority of cases, first-order polynomials were used for baseline subtraction, although fourth-order fits were adopted in some cases. The final cubes were regridded onto 0.3 km s^{-1}-wide velocity channels as our primary data products, but a second version was also produced with 0.5 km s^{-1} channels to increase compatibility with CHIMPS (Rigby et al. 2016) and CHIMPS2 (Eden et al. 2020).

The ^{12}CO (3–2) data were reduced in an almost identical way using ORAC-DR, differing only in the use of a 9-arcsec FWHM Gaussian smooth during the regridding, which results in data cubes whose effective angular resolution matches the 17.2-arcsec resolution of the ^{13}CO and C^{18}O data cubes. Some of the CO data were observed with ACSIS configured with a 1000 MHz bandwidth rather than 250 MHz, which provides a native resolution of 0.42 km s^{-1}, and so the CO data were rebinned to 0.5 km s^{-1} velocity channels throughout for consistency, with the exception of G110, S152, and part of W3, for which the 0.3 km s^{-1} cubes are also available.

Mosaics of each of the regions were produced using KAPPA:WCSMOSAIC with inverse-variance weighting and the `sincsinc` interpolation kernel. The cubes were astrometrically matched such that the C^{18}O and ^{12}CO mosaics share the same pixel grid and size as their ^{13}CO counterparts. The individual reduced data cubes are on the corrected antenna temperature (T_A^*) scale, and we converted the larger mosaics to main beam brightness temperature scale by dividing by the main beam efficiency, $T_{\rm mb} = T_A^*/\eta_{\rm mb}$, where $\eta_{\rm mb} = 0.72$ at 330 GHz, or $\eta_{\rm mb} = 0.61$ at 345 GHz (Buckle et al.

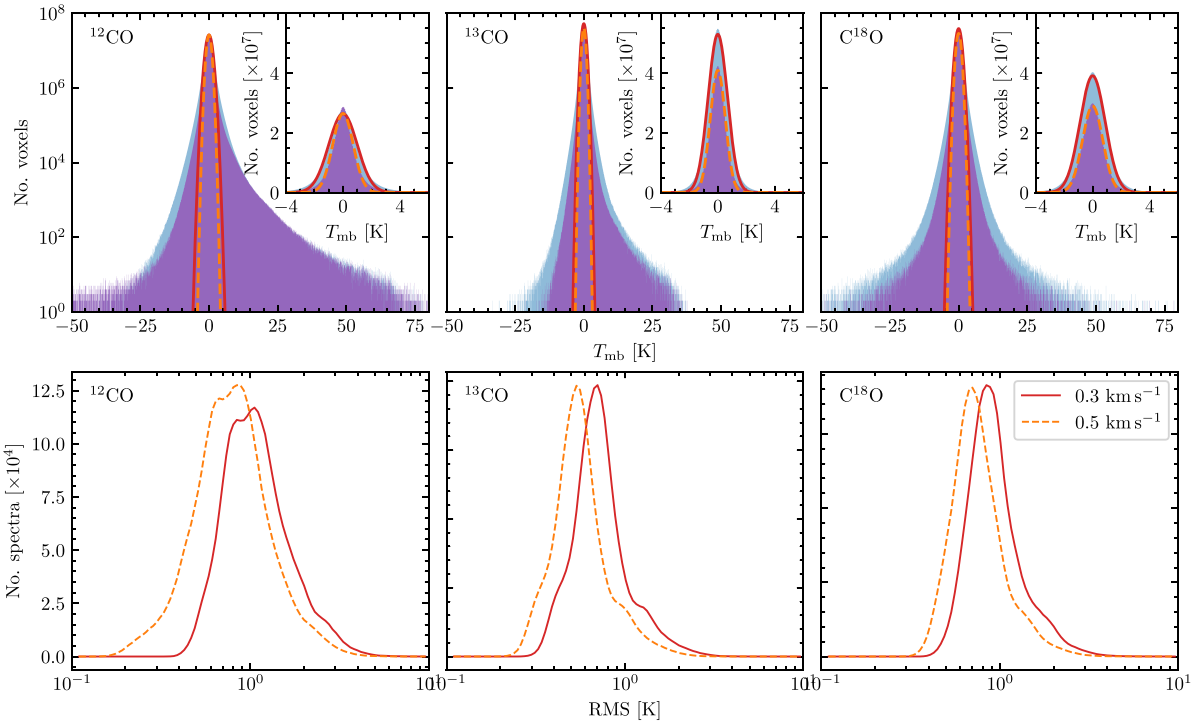

Figure 3. Data quality for ^{12}CO, ^{13}CO, and C^{18}O (3–2) emission in PAMS. *Top row*: Histograms of voxel values in the three transitions with 0.05 K-wide bins. The light and dark-shaded distributions correspond to the 0.3 and 0.5 km s^{-1} channel-width data, respectively. The solid and dashed curves give the best Gaussian fits to the 0.3 and 0.5 km s^{-1} channel-width data, respectively. The inset axes show the same distributions with a linear y-axis. *Bottom row*: Histograms of rms values for the spectra in the ^{12}CO, ^{13}CO, and C^{18}O $J = 3$–2 PAMS data using bins of width 0.02 dex. The 0.3 km s^{-1}-binned and 0.5 km s^{-1}-binned data are shown in solid and dashed lines, respectively.

2009). In Fig. 2 we display a combined view[1] of the ^{12}CO (3–2) emission alongside the PAMS ^{13}CO (3–2) emission for NGC 7538, highlighting the utility of the combined data sets. The regions of orange emission trace the highest column densities of CO, while those of yellow emission trace the diffuse envelope of the region.

2.5 Ancillary data

We make use of the data from the CHIMPS survey (Rigby et al. 2016) directly in Section 4.1, and use the clump catalogue from Rigby et al. (2019) in Section 4.2.

We also use 160 and 250 μm data from Hi-GAL (Molinari et al. 2016) to construct maps of H_2 column density and dust temperature in Section 4.1. These data were reduced using UNIMAP – the University of Rome and IAPS Map Maker–version 5.1.0 (Molinari et al., in preparation), which include de-striping, and the application of photometric offsets determined by comparison to *Planck* data.

3 THE DATA

3.1 Data quality

Fig. 3 shows the distributions of voxels (i.e. 3D pixel) values for the entirety of the PAMS ^{12}CO, ^{13}CO, and C^{18}O (3–2) data, and in both the 0.3- and 0.5-km s^{-1} velocity channel-width variants. To determine a global rms value for each isotopologue, we fitted a normal distribution centred on a value of zero, and recovered rms values of 1.00 (0.72), 0.68 (0.53), and 0.88 (0.71) K in T_{mb} for ^{12}CO, ^{13}CO, and C^{18}O at 0.3 (0.5) km s^{-1}-resolution, respectively. The RMS-equivalent H_2 column densities are $\sim 6 \times 10^{18}$, 3×10^{20}, and 3×10^{21} cm^{-2} for ^{12}CO, ^{13}CO, and C^{18}O (3–2), respectively, assuming optically thin emission with an excitation temperature of 10 K. For these figures, we have assumed abundance ratios of 8.5×10^{-5} for ^{12}CO/H_2 (Frerking, Langer & Wilson 1982), and 79 and 596 for ^{12}CO/^{13}CO and ^{12}CO/C^{18}O, respectively, from Wilson & Rood (1994) evaluated at $R_{GC} = 9.5$ kpc. In all cases, the data are not perfectly normally distributed; the global rms values arise from the central limit theorem when combining a different distribution for each tile within each region. We display the values for each individual region in Table 1. In Fig. 3, the logarithmic *y*-axes allow the non-Gaussian wings of the distributions to be seen most clearly, while the linear *y*-axes in the inset figures demonstrate the overall normal distributions. In ^{12}CO and ^{13}CO, the distributions show significant positive wings associated with the emission. This is less obvious in C^{18}O due to the lower relative abundance of the isotopologue, resulting in a much lower detection rate. The noise levels vary from tile to tile as a result of different observing conditions: zenith opacity (i.e. precipitable water vapour), target elevation, and the number of functioning receptors on HARP. The tile-to-tile noise variations can be seen in Fig. 4, and we display the distributions of noise values for the various PAMS data sets in Fig. 3.

3.2 Emission maps

In Fig. 5, we present the observations of NGC 7538, and equivalent figures for the other regions are shown in Appendix B. We show both the moment 0 (velocity-integrated intensity) maps, and position-

[1]Colour image created using the `multicolorfits` Python package.

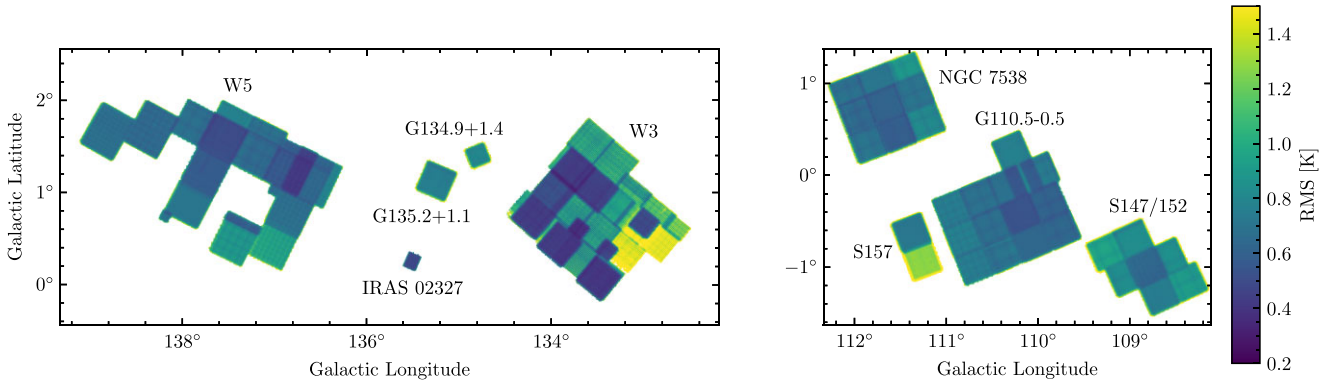

Figure 4. RMS maps for ^{13}CO (3–2) with 0.3 km s^{-1}-wide channels for the $\ell = 137°$ (*left panel*) and $\ell = 110°$ (*right panel*) regions.

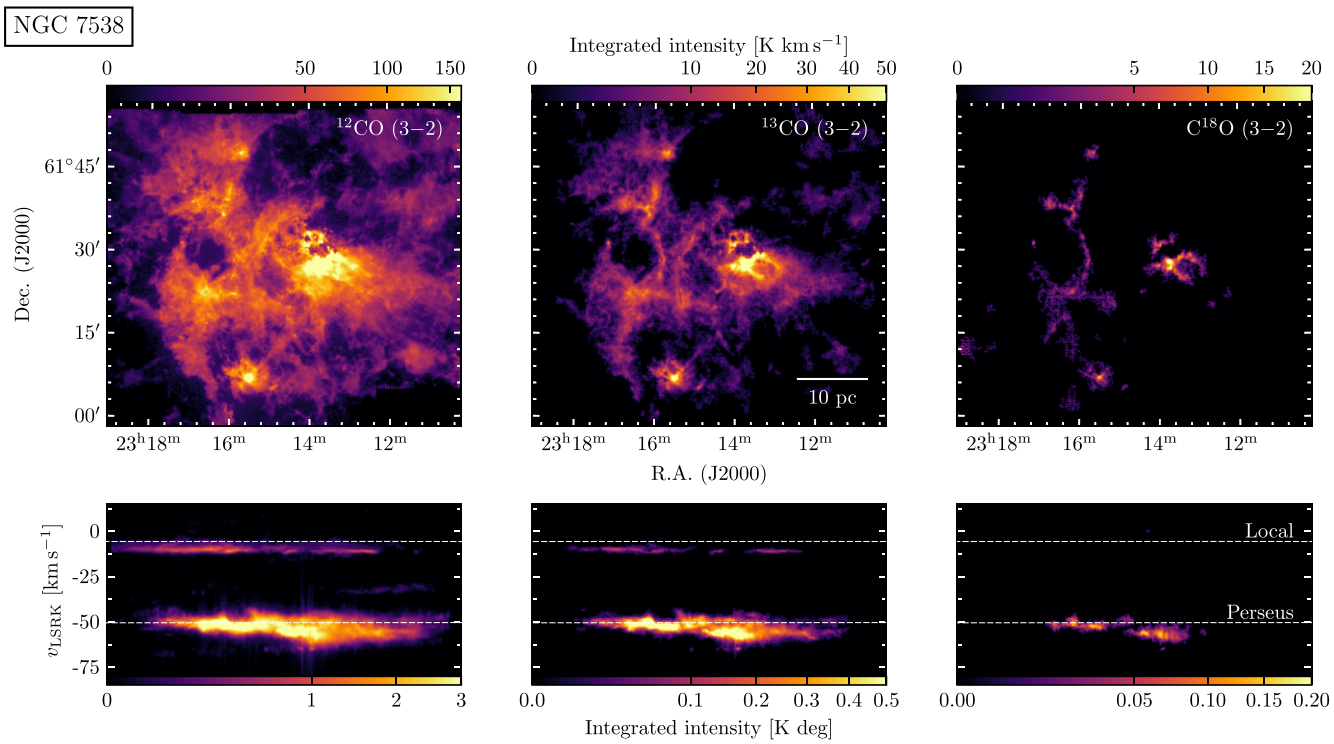

Figure 5. Integrated intensity images of ^{12}CO, ^{13}CO, and C^{18}O (3–2) for NGC 7538, masked using FELLWALKER. *Top row*: Images integrated over the velocity axis. *Bottom row*: Images integrated over the declination axis overlaid with the loci of the spiral arms models of Reid et al. (2019) that are present in this quadrant of the Galaxy and within the PAMS latitude range: the Local Arm, and the Perseus Arm.

velocity maps (declination-integrated intensity) generation for each isotopologue of ^{12}CO. The images were first masked using the FELLWALKER source-extraction software (discussed in Section 3.3). Although the bulk of the emission from NGC 7538 is contained within −70 to −40 km s^{-1}, the region contains a number of outflows that extend beyond this range. The outflows are clearly visible in the position-velocity maps of ^{12}CO and, to a lesser extent, ^{13}CO. The field also contains a minor secondary emission component between −17 and −3 km s^{-1}, which contains just 8 and 1 per cent of the total emission in ^{12}CO and ^{13}CO (3–2), respectively.

With the lowest *effective* critical density, the ^{12}CO (3–2) emission traces the most diffuse component of the molecular cloud, which fills much of the field of view, and it is especially powerful for tracing outflows. By contrast, the ^{13}CO and C^{18}O (3–2) emission traces higher density components; ^{12}CO is ≈ 80 and 600 times more abundant than ^{13}CO and C^{18}O, respectively, at a Galactocentric distance of 9.5 kpc (Wilson & Rood 1994), and so the rarer isotopologues have substantially lower optical depths. Rigby et al. (2019) found that ^{13}CO (3–2) emission within molecular clouds in the inner Milky Way is predominantly $\tau < 1$, and only becomes optically thick towards the densest ∼1 pc-scale clumps; only 3 per cent of clumps in the CHIMPS sample have mean optical depths greater than 1. NGC 7538 and the other PAMS regions also reside substantially further out in the Galaxy than the clumps typically targeted by CHIMPS, and so optical depths are likely to be even lower for PAMS. ^{13}CO (3–2) emission is therefore expected to be a reasonably good tracer of H_2 column density where it is detected in these regions.

In Fig. 5 we also overlay the loci of the models of the two spiral arms of Reid et al. (2019) that are present in this quadrant of the Galaxy, which fall within the PAMS latitude range. We clearly detect emission associated with the Local Arm in addition to the expected Perseus Arm – with which the main PAMS regions are associated. The Reid et al. (2019) models are based upon trigonometric parallaxes of ∼200 high-mass star-forming regions, obtained by the Bar and Spiral Structure Legacy (BeSSeL) Survey[2] and the Japanese VLBI Exploration of Radio Astrometry (VERA) project[3] which are known to a high level of accuracy. NGC 7538 clearly resides within the Perseus arm, and the secondary emission component is consistent with a position in the Local Arm.

3.3 Source extraction

A series of source extractions was performed upon the ^{13}CO (3–2) PAMS data using the FELLWALKER (Berry 2015) algorithm, which is part of CUPID (Berry et al. 2007). FELLWALKER is a watershed clump-finding algorithm which segments our arrays of voxels into discrete clumps of emission, each of which contains a significant emission peak. FELLWALKER assigns all voxels brighter than a threshold level, determined by the noise, to a single clump in this way. In addition to producing a catalogue, it also generates a mask which has the same dimensions as the input array, but in which each voxel value corresponds to the ID of a catalogued clump. We refer to these masks as 'assignment masks' hereafter, and these may also be used to effectively remove the background from the data cubes, amongst other useful applications.

Source extraction was performed upon the signal-to-noise ratio (SNR) mosaics of each region. Initial tests showed that FELLWALKER was much more effective at locating the emission present within the data when running over the SNR cubes as opposed to the $T_{\rm mb}$ cubes, resulting in a smaller amount of emission remaining in the residual cubes. After an initial source search on the SNR cubes using CUPID:FINDCLUMPS, the CUPID:EXTRACTCLUMPS algorithm then uses the FELLWALKER-defined mask to extract information from the $T_{\rm mb}$ cubes, recalculating properties such as the intensity-weighted centroid and peak coordinate of each source, which is different in $T_{\rm mb}$-space compared with SNR-space. A further advantage is that an extraction of sources on the SNR cubes reduces the instances of false-positive detections which can arise as a consequence of noisy spectra at the image edges or at the seams of the mosaics.

A total of three source extractions were run, with the following purposes:

(i) `fwhires`: Our primary source extraction, which was configured to locate objects on the 'clump' size-scale, allowing localized levels of fragmentation.

(ii) `fwlores`: This setup essentially identifies the same pixels of emission as `fwhires`, but was configured to retain the largest structures within each field.

(iii) `fwchimps`: A reference extraction was run with a set of parameters optimized to recover, as closely as possible, a catalogue that is consistent with the CHIMPS survey whose extraction was described in Rigby et al. (2016) and analysed in Rigby et al. (2019).

For both `fwhires` and `fwlores`, source extraction was performed on the 0.3-km s^{-1}-resolution mosaics, essentially giving the 'best' case for our PAMS data, while the `fwchimps` extraction was conducted on the 0.5 km s^{-1}-resolution mosaics to facilitate a more direct comparison with CHIMPS. These source extractions were also performed after smoothing the data to a resolution of 22.0 arcsec, which was found to be the best compromise between retaining relatively high resolution, while improving the noise statistics. For these extractions, the minimum height of a peak to be included was set to SNR = 3, and the noise level was set to SNR = 1, meaning that all contiguous pixels down to the rms value are considered to be part of each source. Although the noise level (i.e. minimum voxel value to be included in a clump) is rather low, we found that higher levels for this parameter led to considerably more emission in the residuals. As always, flux boosting will be present in the low-SNR sources, and we stress that this extraction has been tuned to maximize the recovery of the emission, as opposed to catalogue robustness (i.e. minimizing false positives). The difference in the `fwhires` and `fwlores` was achieved by setting different values of `MinDip` which was set to an SNR value of 5 in the `fwhires` case, and 1000 in the `fwlores` case. By contrast, the `fwchimps` extraction was configured to use the parameters described in Rigby et al. (2016), with the exception that the `RMS` parameter was set to 1.7, reflecting the lower sensitivity of the CHIMPS data after smoothing to the same resolution of 27.4 arcsec that was originally used. One further difference in the process is that this extraction identifies sources at a resolution of 27.4 arcsec, but then extracts the parameters at the native resolution of 17.2 arcsec (15.2 arcsec in the original CHIMPS extraction). Both PAMS extractions identify and extract source parameters at the same resolution of 22.0 arcsec. We list the full set of FELLWALKER parameters used for each setup in Appendix C.

While FELLWALKER does not nominally contain any information about the hierarchical structure of the emission, our twin `fwhires` and `fwlores` allow some aspects of this to be recovered. Both extractions identify the same pixels of emission, and differ only in the assignment to catalogued structures. Because of this, we are able to assign every clump within the `fwhires` extraction to a larger structure from the `fwlores` extraction, and thus restore some information about the hierarchy. By contrast, the SCIMES (Colombo et al. 2015) algorithm is based upon the ASTRODENDRO implementation of dendrograms (Rosolowsky et al. 2008), which identify substructures that are significant in terms of brightness and area based upon contour levels. While dendrograms also keep track of compact sources (identified as *leaves* by analogy) inside larger substructures (*branches*) of molecular clouds (*trunks*), their individual values may differ compared with the equivalent FELLWALKER-defined clumps, but statistically the two approaches return compatible results (Rani et al. 2023). In this paper, we use FELLWALKER to enable a direct comparison with the properties of the clump population identified within the CHIMPS survey of Rigby et al. (2019) in the Inner Galaxy.

Table 2 contains the first five rows of the `fwhires` catalogue, with selected information given. We make full versions of the `fwlores`, `fwhires`, and `fwchimps` catalogues available alongside this paper, and we detail the column descriptions in Appendix D. The format of the three catalogues is almost identical, with the exception that the `fwhires` catalogue also lists the ID of the parent source in the `fwlores` catalogue to allow the hierarchical information about the larger complexes to be retained.

Fig. 6 illustrates the differences between the source-extraction setups. The 2D representations of the FELLWALKER masks clearly show the difference between the `fwhires` and `fwlores` extractions, illustrating that the same pixels of emission are recovered, but differ in their assignment to different structures. The `fwchimps` extraction

[2] http://bessel.vlbi-astrometry.org/
[3] https://www.miz.nao.ac.jp/veraserver/

Table 2. Information about sources extracted from the `fwhires` source extraction. The columns give the IAU-compliant designation, the PAMS region, source ID in assignment cube, centroid longitude, centroid latitude, centroid velocity, velocity dispersion, equivalent radius, sum of ^{13}CO pixel values, peak ^{13}CO pixel value, peak signal-to-noise ratio, and ID of parent source in corresponding `fwlores` extraction. The first five rows, and selected columns only are included here for illustrative purposes. The full catalogue, along with the full `fwlores` and `fwchimps` catalogues, are available in machine-readable format, as detailed in the Data Availability section.

Designation	Region	ID	ℓ °	b °	$v_{\rm lsr}$ km s^{-1}	$\sigma(v_{\rm lsr})$ km s^{-1}	$R_{\rm eq}$ arcsec	Sum $T_{\rm mb}$ K	Peak $T_{\rm mb}$ K	Peak S/N	Parent ID
G110.224+00.069	G110	1	110.22371	0.06935	−53.09	0.89	38.4	44592.5	20.8	45.6	1
G110.122+00.087	G110	2	110.12224	0.08703	−51.03	1.08	49.8	127261.3	21.9	44.2	1
G109.982−00.072	G110	3	109.98246	−0.0716	−51.06	0.64	42.6	18207.2	16.2	37.9	1
G110.194+00.012	G110	4	110.19398	0.01226	−50.41	1.58	40.3	44889.0	17.3	31.1	1
G110.301+00.003	G110	5	110.30127	0.00345	−52.75	0.72	31.4	20078.0	14.1	29.9	1

shows the substantial difference that the data quality makes in source extraction, and the necessity to have a like-for-like extraction in order to make meaningful comparisons to other data sets that take into account biases resulting from sensitivity. Both `fwhires` and `fwlores` recover much fainter emission than `fwchimps`, which exists in the diffuse envelopes of the molecular clouds. The residual images give an idea of how complete the various extractions are. While `fwhires` and `fwlores` leave almost no visible residual in the integrated position–position intensity maps, those extractions still leave faint and unrecovered emission that is most clearly visible in the residual integrated position–velocity intensity maps.

4 RESULTS

4.1 CO-to-H_2 conversion factors

The $X_{\rm CO}$ factor converts the integrated intensity of CO emission in a particular transition (and a particular isotopologue) to total molecular-hydrogen column density. In its general form:

$$N({\rm H_2}) = X_{\rm CO}\, W({\rm CO}), \tag{1}$$

where $N({\rm H_2})$ is the molecular-hydrogen column density, and $W({\rm CO})$ is the integrated intensity of ^{12}CO (1–0) emission. For reference, Bolatto, Wolfire & Leroy (2013) recommend a typical value of $X_{\rm CO} = 2 \times 10^{20}$ cm^{-2} (K km s^{-1})$^{-1}$ in the Milky Way disc. $X_{\rm CO}$ condenses the wide range of environmentally varying excitation conditions that are likely to be found within a relatively large area of Galactic disc (typically used in external galaxies) into a single scaling relationship. Here, we explore the value of $X_{\rm CO}$ for our ^{12}CO and ^{13}CO (3–2) emission lines (which we refer to as $X_{^{12}{\rm CO\,(3-2)}}$ and $X_{^{13}{\rm CO\,(3-2)}}$, respectively) within PAMS, and compare the results with those derived from similar data in an Inner Galaxy field. The Inner Galaxy region we used is centred at $\ell = 30°$ – which contains the massive star-forming complex W43 and cloud G29.96−0.02–using mosaics of the ^{12}CO COHRS (Dempsey et al. 2013; Park et al. 2023) and ^{13}CO (3–2) CHIMPS data (Rigby et al. 2016). The latter were re-processed for the CHIMPS2 Inner Galaxy survey (Rigby et al., in preparation) on 6 arcsec pixels, with an effective resolution matching PAMS.

To calculate $X_{\rm CO}$ values, we compared the moment 0 (velocity-integrated intensity) maps to maps of H_2 column density derived from greybody fitting with 160 and 250 μm imaging from the *Herschel*/Hi-GAL survey following the method of Peretto et al. (2016). The specific intensity I at a frequency ν is related to H_2 column density via

$$I_\nu = \mu_{\rm H_2} m_{\rm H} N({\rm H_2}) \gamma^{-1} \kappa_0 \left(\frac{\nu}{\nu_0}\right)^{\beta} B_\nu(T_{\rm d}), \tag{2}$$

where $\mu_{\rm H_2}$ is the mean molecular mass per H_2 (equal to 2.8 for molecular gas with a relative Helium abundance of 25 per cent), $m_{\rm H}$ is the mass of a hydrogen atom, γ is the gas-to-dust mass ratio, κ_ν is the dust opacity at a reference frequency of ν_0, $B_\nu(T_{\rm d})$ is the value of the Planck function evaluated at frequency ν for the dust temperature $T_{\rm d}$. First, maps of dust temperature are determined from the ratio of 160 to 250 μm flux densities after convolving the former to 18-arcsec resolution to match the latter:

$$\frac{I_{\nu_{160}}}{I_{\nu_{250}}} = \left(\frac{250}{160}\right)^{\beta} \left(\frac{B_{\nu_{160}}(T_{\rm d})}{B_{\nu_{250}}(T_{\rm d})}\right), \tag{3}$$

for which we adopt $\beta = 2$, and sample dust temperatures to the nearest 0.01 K. We then generate maps of column density using the corresponding 250 μm map:

$$N({\rm H_2}) = \frac{I_{\nu_{250}} \gamma}{\mu_{\rm H_2} m_{\rm H} \kappa_0 \left(\frac{\nu}{\nu_0}\right)^{\beta} B_\nu(T_{\rm d})}, \tag{4}$$

using a value of $\kappa_0 = 12.0$ cm^2 g^{-1} at 250 μm,[4] and a typical gas-to-dust mass ratio of $\gamma = 100$.

The ^{12}CO and ^{13}CO cubes, and H_2 column-density maps were then smoothed to a common angular resolution of 20 arcsec, and the cubes were integrated over velocity ranges containing the emission to produce moment 0 (integrated intensity) maps. We masked the moment 0 maps below a contour level determined for each region in order to limit the impact of noise. The H_2 column-density maps were then resampled onto the same pixel grid as the moment 0 images so that the column densities and integrated intensities could be compared on a pixel-by-pixel basis. The overlap between Hi-GAL and PAMS meant that we could calculate $X_{\rm CO}$ factors for around 70 per cent of the survey area with S152, S157, and most of G110 falling out of the Hi-GAL coverage (see Fig. 1).

We performed several calculations of $X_{^{12}{\rm CO\,(3-2)}}$ and $X_{^{13}{\rm CO\,(3-2)}}$ for our regions using different methods;

(i) We used equation (1), and performed a least-squares fit to the data points;

(ii) We adapted the first approach to include a column-density offset (i.e. background correction):

$$N({\rm H_2}) = X_{\rm CO}\, W({\rm CO}) + N({\rm H_2})_{\rm bg}; \tag{5}$$

(iii) We calculated the median value of the individual $X_{\rm CO}$ pixel values;

[4]The dust opacity is interpolated from table 1, column 5 of Ossenkopf & Henning (1994), but scaled down by a factor of 1.5, which was found by Kauffmann et al. (2010) to better reproduce extinction measurements.

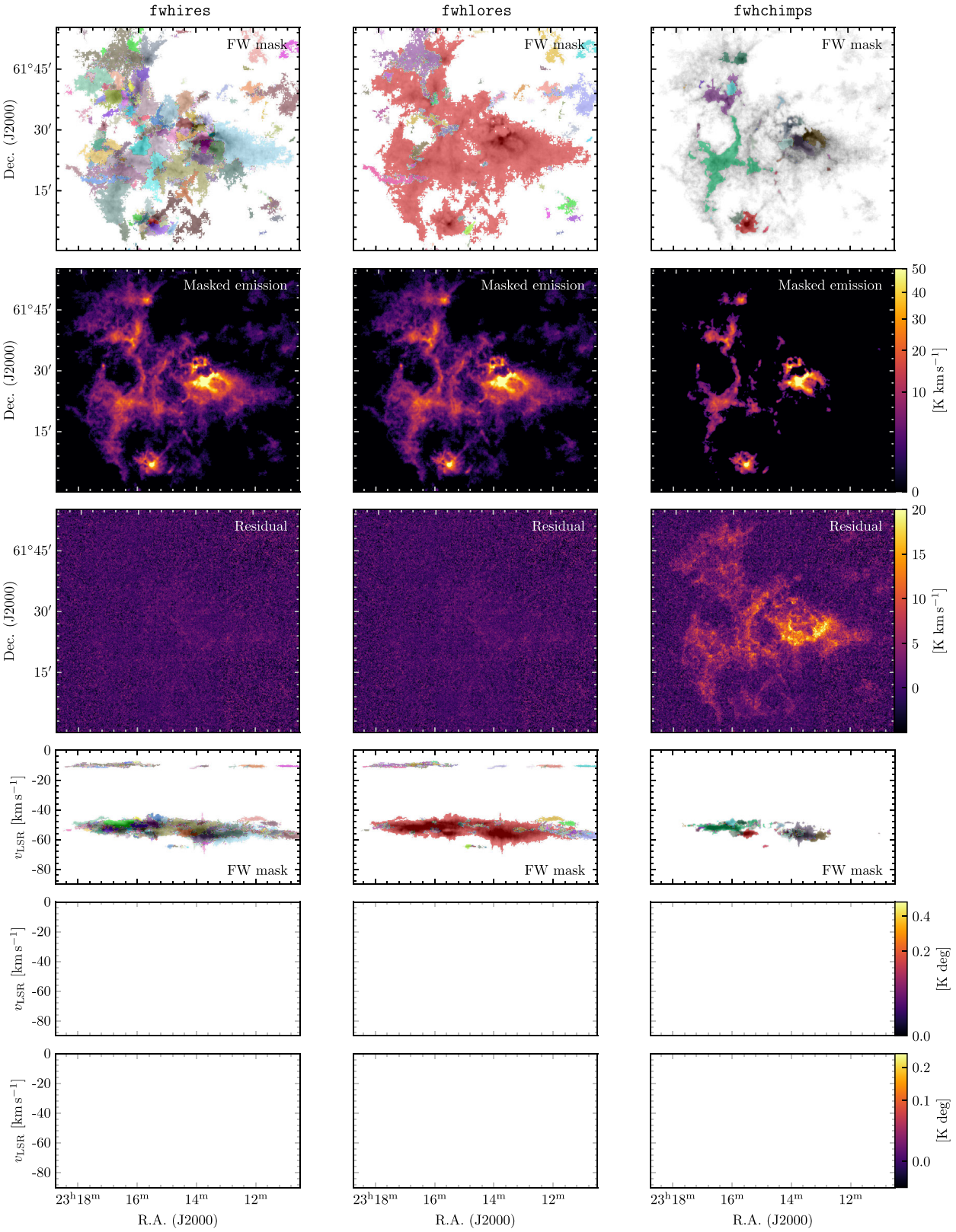

Figure 6. Each column of images shows different aspects of the `fwhires`, `fwlores`, and `fwchimps`FELLWALKER source–extraction setups. *Top row*: A greyscale representation of the ^{13}CO (3–2) velocity-integrated intensity map of NGC 7538 overlaid with 2D representations of the FELLWALKER masks. *Second row*: Velocity-integrated intensity images from the FELLWALKER-masked cubes. *Third row*: Residual velocity-integrated intensity map. *Fourth row*: A greyscale representation of the ^{13}CO (3–2) declination-integrated position-velocity map overlaid with 2D representations of the FELLWALKER masks. *Fifth row*: Declination-integrated position-velocity maps of the masked cubes. *Bottom row*: Residual declination-integrated position-velocity maps of the masked intensity. The images in each row are all on the same intensity scale, indicated by the colour bar on the right-most image.

Table 3. $X_{\rm CO}$ values for ^{12}CO (3–2) in the various regions, with values listed for Methods (i)–(iv) outlined in Section 4.1. For Method (ii) the background column-density value, $N(H_2)$, is also listed. For Method (iii) the uncertainties indicate the 16th–84th percentile range.

Region	(i) $X_{^{12}\rm CO\,(3-2)}$ $\rm cm^{-2}\,(K\,km\,s^{-1})^{-1}$	(ii) $X_{^{12}\rm CO\,(3-2)}$ $\rm cm^{-2}\,(K\,km\,s^{-1})^{-1}$	$N(H_2)_0$ $\rm cm^{-2}$	(iii) $X_{^{12}\rm CO\,(3-2)}$ $\rm cm^{-2}\,(K\,km\,s^{-1})^{-1}$	(iv) $X_{^{12}\rm CO\,(3-2)}$ $\rm cm^{-2}\,(K\,km\,s^{-1})^{-1}$
G110	2.7×10^{20}	1.8×10^{20}	2.8×10^{21}	$4.0^{+1.8}_{-1.4} \times 10^{20}$	3.4×10^{20}
G135	1.4×10^{20}	5.4×10^{19}	2.8×10^{21}	$2.8^{+3.9}_{-1.5} \times 10^{20}$	2.1×10^{20}
IRAS 02327	3.1×10^{20}	2.0×10^{20}	2.6×10^{21}	$4.9^{+3.8}_{-2.1} \times 10^{20}$	4.0×10^{20}
NGC 7538	2.5×10^{20}	2.3×10^{20}	1.6×10^{21}	$3.2^{+3.2}_{-1.3} \times 10^{20}$	2.8×10^{20}
W3	2.2×10^{20}	1.5×10^{20}	4.0×10^{21}	$3.4^{+1.3}_{-1.1} \times 10^{20}$	3.0×10^{20}
W5	2.5×10^{20}	1.5×10^{20}	3.2×10^{21}	$4.5^{+3.1}_{-2.3} \times 10^{20}$	3.5×10^{20}
Inner Galaxy	4.0×10^{20}	3.0×10^{20}	9.1×10^{21}	$4.3^{+1.9}_{-1.0} \times 10^{20}$	4.2×10^{20}
Outer Galaxy	2.5×10^{20}	2.3×10^{20}	1.7×10^{21}	$3.4^{+2.9}_{-1.4} \times 10^{20}$	2.9×10^{20}
All	3.8×10^{20}	3.4×10^{20}	3.7×10^{21}	$4.1^{+2.1}_{-1.3} \times 10^{20}$	4.0×10^{20}

(iv) We calculated a global average as:

$$X_{\rm CO} = \frac{\sum_i N(H_2)_i}{\sum_i W(CO)_i}. \quad (6)$$

We summarize these results in Tables 3 and 4. for ^{12}CO (3–2) and ^{13}CO (3–2), respectively.

We show the distributions of $X_{\rm CO}$ pixel values across PAMS in Fig. 7, in which it is apparent that the Outer Galaxy values are lower than the Inner Galaxy values for both ^{12}CO and ^{13}CO (3–2), with the discrepancy being larger for the latter. Fig. 8 illustrates several additional aspects of these results by exploring the correlation between individual $X_{\rm CO}$ pixel values and other properties. In Panels (a) and (d), we show the distributions of pixel values of H_2 column density as functions of the integrated intensity of ^{12}CO and ^{13}CO (3–2) in the corresponding pixel. In both cases, it is clear that the distributions are not completely linear (i.e. simple power laws in log-space) and there is considerable scatter. We see a flattening of the distributions at low integrated intensity that is more prominent in ^{12}CO, and indicative of the column-density background that is detected in the spaced-based *Herschel* observations, but not discernible in the ground-based CO observations due to their sensitivity. At the bright end of the distributions, the column density also curves upwards – and this behaviour is stronger in ^{12}CO (3–2) – indicating a saturation of CO emission as a consequence of the emission becoming optically thick at the highest column densities. The global $X_{\rm CO}$ values (Method iv) are plotted as black lines, and these are the values that are representative of the kind of $X_{\rm CO}$ values that are used in studies of extragalactic systems, where star-forming complexes may be unresolved. The scatter around the global values is clearly not random, and we explore the origin by examining the $X_{\rm CO}$ distributions as functions of dust temperature and column density in Panels (b), (c), (e), and (f).

The distributions of individual $X_{\rm CO}$ values are very broad, spanning between one and two orders of magnitude in both isotopologues. For all cases, the distributions of dust temperature are also broad for a given $X_{\rm CO}$ value. One very noticeable trend is that the lower envelope of the dust temperature distribution is ∼5 K higher in the Inner Galaxy samples (contours). It is also of particular note that the peak of the distribution of $X_{^{13}\rm CO\,(3-2)}$ values in the Inner Galaxy is a factor of ∼2–3 higher than the global $X_{^{13}\rm CO\,(3-2)}$ value for the Outer Galaxy, suggesting that global values of $X_{\rm CO}$ are likely to be weighted towards particular ISM conditions that are conducive to bright CO emission, but which are not representative of typical conditions by area.

For $X_{^{12}\rm CO\,(3-2)}$, the range of values returned from our different methods are fairly comparable, ranging between 2.3 and $4.2 \times 10^{20}\,\rm cm^{-2}\,(K\,km\,s^{-1})^{-1}$. Each of the methods systematically returns a higher value of $X_{^{12}\rm CO\,(3-2)}$ for the Inner Galaxy than for the Outer Galaxy region although the distributions overlap substantially (see Fig. 7). Given the different calculation methods, we suggest that – in principle – our Method (i) values are most appropriate for resolved studies, and Method (iv) values are more appropriate for unresolved studies. Given the insignificant difference for ^{12}CO (3–2), we recommend the usage of $X_{^{12}\rm CO\,(3-2)} = 4.0 \times 10^{20}\,\rm cm^{-2}\,(K\,km\,s^{-1})^{-1}$ for both resolved studies and unresolved studies, noting that range of values varies by around ±50 per cent (as per Method iii). This is in excellent agreement with Colombo et al. (2019) who derived by their value by applying an average 3–2/1–0 line-ratio measurement to the Bolatto et al. (2013) $X_{\rm CO}$ value listed above using the wider COHRS data set of which we take a subset for our Inner Galaxy sample.

The picture is more varied for $X_{^{13}\rm CO\,(3-2)}$, with values between 2.2 and $7.0 \times 10^{21}\,\rm cm^{-2}\,(K\,km\,s^{-1})^{-1}$ across the different regions and calculation methods. All four methods return higher values in the Inner Galaxy than in the Outer Galaxy by a factor of ∼2–3. The higher column-density background in the Inner Galaxy, which arises as a consequence of the greater number of spiral arms present along the line of sight and a greater column of Galactic disc, appears to be the primary driver of the different recovered values. This variation is clearly illustrated in Fig. 8(d) where the global average lines (for Method iv) are more widely separated for the Inner and Outer Galaxy. The peak of the $X_{^{13}\rm CO\,(3-2)}$ distributions in Figs 7, 8(e) and (f) between the Inner and Outer Galaxy are noticeably different. In the Inner Galaxy, it appears that the higher dust-temperature background of ∼20 K compared with ∼17 K in the Outer Galaxy, along with a higher background of column density contribute to the higher $X_{^{13}\rm CO\,(3-2)}$ values. The single dust temperature is less likely to represent the underlying gas conditions at this Inner Galaxy position, where a greater fraction of the Galactic disc is located within the column. We note that gas and dust temperatures are only likely to be coupled at densities greater than $\sim n(H_2) > 10^{4.5}\,\rm cm^{-3}$ (Goldsmith 2001), so that for much of the gas in molecular clouds – especially their envelopes – the CO excitation temperature is unlikely to follow the dust temperature. We will explore CO excitation temperatures, along with a local

Table 4. $X_{\rm CO}$ values for ^{13}CO (3–2) in the various regions, with values listed for Methods (i)–(iv) outlined in Section 4.1. For Method (ii) the background column-density value, $N(H_2)$, is also listed. For Method (iii) the uncertainties indicate the 16th–84th percentile range.

Region	(i) $X_{^{13}{\rm CO}\,(3-2)}$ $\rm cm^{-2}\,(K\,km\,s^{-1})^{-1}$	(ii) $X_{^{13}{\rm CO}\,(3-2)}$ $\rm cm^{-2}\,(K\,km\,s^{-1})^{-1}$	$N(H_2)_0$ $\rm cm^{-2}$	(iii) $X_{^{13}{\rm CO}\,(3-2)}$ $\rm cm^{-2}\,(K\,km\,s^{-1})^{-1}$	(iv) $X_{^{13}{\rm CO}\,(3-2)}$ $\rm cm^{-2}\,(K\,km\,s^{-1})^{-1}$
G110	2.2×10^{21}	1.5×10^{21}	5.3×10^{21}	$2.3^{+1.3}_{-0.9} \times 10^{21}$	2.4×10^{21}
G135	1.4×10^{21}	6.4×10^{20}	2.6×10^{21}	$1.6^{+0.8}_{-0.5} \times 10^{21}$	1.6×10^{21}
IRAS 02327	2.5×10^{21}	1.9×10^{21}	2.4×10^{21}	$3.2^{+1.2}_{-1.0} \times 10^{21}$	2.9×10^{21}
NGC 7538	2.4×10^{21}	2.2×10^{21}	2.2×10^{21}	$2.5^{+1.1}_{-0.9} \times 10^{21}$	2.5×10^{21}
W3	1.2×10^{21}	7.8×10^{20}	8.1×10^{21}	$2.2^{+1.2}_{-1.0} \times 10^{21}$	2.0×10^{21}
W5	1.8×10^{21}	1.5×10^{21}	2.3×10^{21}	$2.0^{+1.2}_{-0.8} \times 10^{21}$	2.0×10^{21}
Inner Galaxy	4.8×10^{21}	3.0×10^{21}	2.1×10^{22}	$7.0^{+2.9}_{-2.5} \times 10^{21}$	6.0×10^{21}
Outer Galaxy	2.4×10^{21}	2.2×10^{21}	1.8×10^{21}	$2.4^{+1.1}_{-0.9} \times 10^{21}$	2.5×10^{21}
All	4.3×10^{21}	2.9×10^{21}	1.7×10^{22}	$6.1^{+3.3}_{-3.3} \times 10^{21}$	5.3×10^{21}

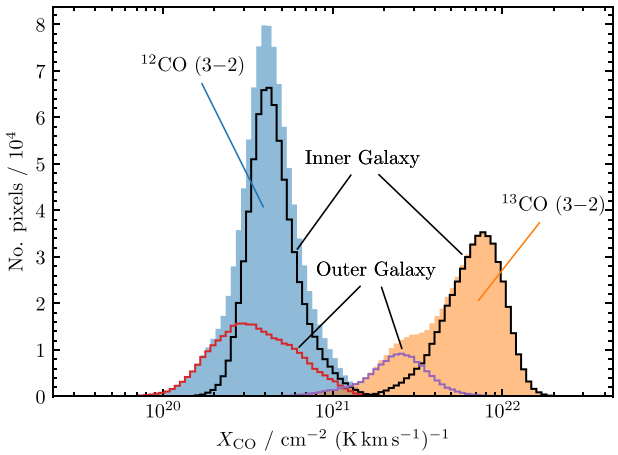

Figure 7. Histograms comparing the distributions of $X_{\rm CO}$ for ^{12}CO and ^{13}CO (3–2) for the all pixels (shaded), and for the Inner and Outer Galaxy subsamples. The ^{13}CO (3–2) histogram has been scaled up by a factor of 2 for illustrative purposes.

thermodynamic equilibrium (LTE)-based $X_{\rm CO}$ derivation in a future paper.

For resolved studies, we recommend the usage of our Method (i) value of 4.3×10^{21} cm^{-2} (K km s^{-1})$^{-1}$ as a representative value for $X_{^{13}{\rm CO}\,(3-2)}$, and for unresolved studies, we recommend a value of 5.3×10^{21} cm^{-2} (K km s^{-1})$^{-1}$. As for ^{12}CO, these $X_{\rm CO}$ factors should always be used with the knowledge that their derivation is biased towards (relatively) hot high-column-density gas where CO is brightest on large scales, but will not accurately account for column densities in other environments. It is also important to recognize that a Galactic gradient of $X_{\rm CO}$ values is evident in our data, which we will discuss further in Section 5. In all cases, we recommend that a multiplicative factor of 1.5 be adopted for the uncertainty in the $X_{\rm CO}$ values to encapsulate the 1-σ spread of the values.

4.2 Molecular-cloud properties

In this section, we explore some of the basic properties of molecular-cloud structures within PAMS, and compare those with an Inner Galaxy reference from the CHIMPS survey (Rigby et al. 2019). The reference sample was restricted to include only those clouds with distances between 2 and 4 kpc which approximately matches the range in distance of the PAMS sources and thus limits the effect of distance biases. Since CHIMPS covers a longitude range of $28^\circ \lesssim \ell \lesssim 46^\circ$, the distance limitation results in the Inner Galaxy sample covering a range in Galactocentric radius of $5 \lesssim R_{\rm GC} \lesssim 7$ kpc, compared with roughly 9–10 kpc for the PAMS Outer Galaxy sample. We also applied a minimum peak SNR criterion to all of our catalogues in order to emulate the 'reliability' flagging that was made in the CHIMPS catalogue. In the CHIMPS catalogue, 95 per cent of sources with the highest reliability flags have a peak SNR greater than 9 and, similarly, 95 per cent of sources with the lowest reliability flag have a peak SNR less than 9, and so we adopt this value for our cut. This conservative cut helps eliminate potentially spurious sources that FELLWALKER can produce at low SNR, which often appear as separated islands of low-intensity emission (which we refer to as 'archipelagos'). We adopt the same cut for the CHIMPS Inner Galaxy sample (as opposed to using the reliability flags directly) for consistency. By applying these cuts, the `fwhires`, `fwlores`, `fwchimps`, and Inner Galaxy catalogues were reduced from 948, 483, 231, and 4999 sources to 499, 80, 140, and 865 sources, respectively.

4.2.1 *Source radii*

There are several ways of reporting the size of molecular clouds, which each have drawbacks due to the intrinsic difficulty of representing the complex morphologies and intensity distributions with simple metrics that can be given in a catalogue. These differences may have implications for the way in which key scaling relationships, such as the size–linewidth relationship (Larson 1981), are compared between different data sets and so we explore two of them briefly here.

The intensity-weighted radius, R_σ, is given by:

$$R_\sigma = d\,\sqrt{\sigma_x \sigma_y}, \tag{7}$$

where d is the source distance and σ_x and σ_y are the intensity-weighted rms dispersions in the x- and y-axes of the image (in the case of PAMS, R.A. and Dec., respectively), deconvolved by the effective beam size. In the case of a perfect Gaussian source detected at a high signal-to-noise ratio, R_σ would give the standard deviation of the source profile, equivalent to the FWHM/$\sqrt{8 \ln 2}$. An alternative is the radius of a circle with the equivalent angular area, A, of the source. The equivalent radius is:

$$R_{\rm eq} = d\,\sqrt{A/\pi}. \tag{8}$$

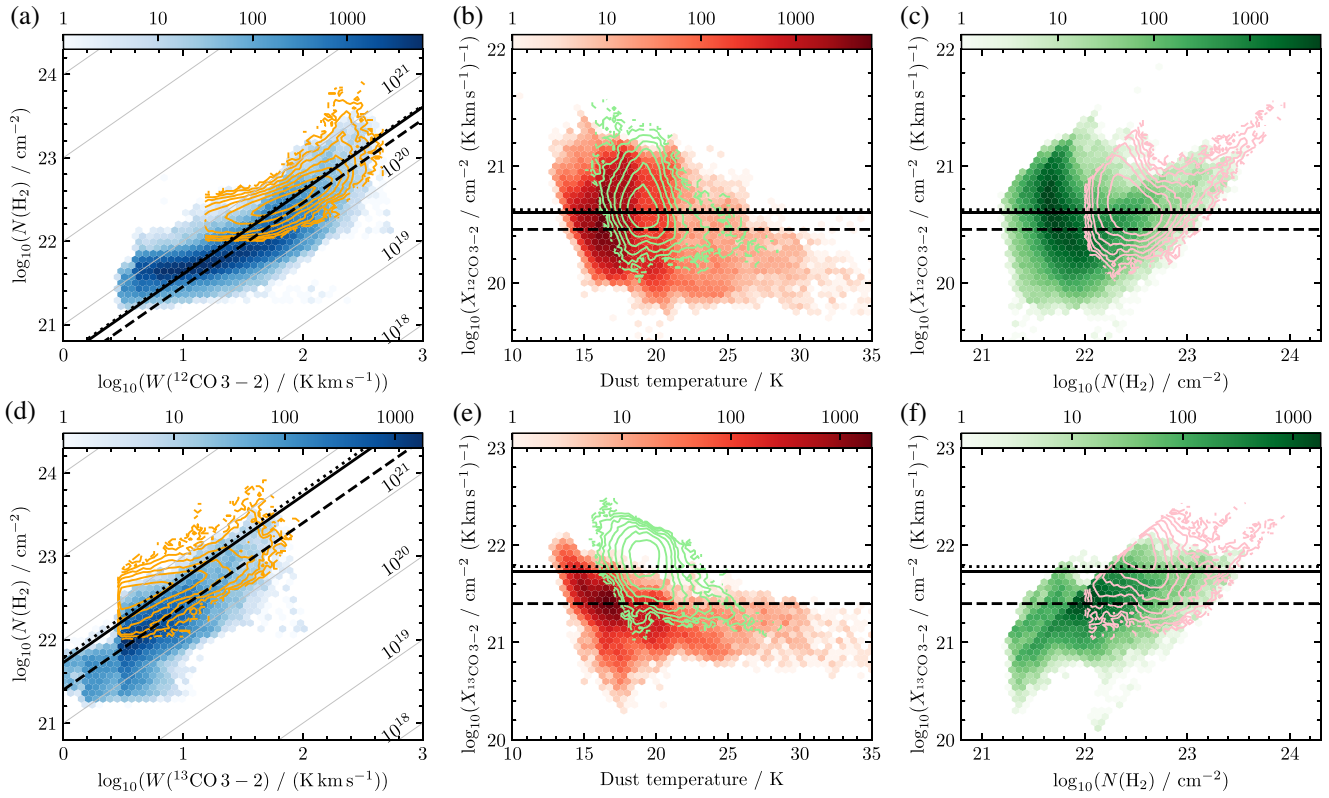

Figure 8. 2D histograms comparing the pixel-by-pixel distributions of: (*left column*) H_2 column density as a function of integrated intensity; (*middle column*) X_{CO} as a function of dust temperature; (*right column*) X_{CO} as a function of H_2 column density. The top and bottom rows examine the distributions for ^{12}CO and ^{13}CO (3–2) emission, respectively. In each case, the hexagonal histograms show the values for the Outer Galaxy regions, while the logarithmically spaced contours represent the Inner Galaxy region. The solid, dotted, and dashed lines in each panel show the global values [Method (iv) from Section 4.1] of X_{CO} derived for the combined, Inner Galaxy, and Outer Galaxy samples, respectively.

Again, the angular radius must first be deconvolved by the effective beam size before scaling to the relevant distance. We also define

$$\eta_R = R_{\rm eq}/R_\sigma \tag{9}$$

to capture the ratio of the two measurements. These two radii differ in approach because R_σ depends upon the intensity distribution of the source, while $R_{\rm eq}$ depends only upon the area of the footprint of the source. A cloud with a compact and bright centre surrounded by diffuse emission will therefore have a much smaller value of R_σ than $R_{\rm eq}$. $R_{\rm eq}$ is more easily impacted by the sensitivity of the observations, and will recover larger values in deeper observations that detect more diffuse emission. By contrast R_σ varies less across observations of different sensitivity and so we generally favour this prescription (and indeed η_R is weakly correlated with peak SNR). Making both measurements of the radius will allow maximum compatibility with other measurements in the literature which use either method, and environmental trends may also reveal themselves in the relationship between these two measurements.

In Fig. 9 we show the relationship between R_σ and $R_{\rm eq}$ for our various FELLWALKER source extractions along with their η_R distributions, and with a comparison to the values reported by Rigby et al. (2019) for the Inner Galaxy from the distance-limited CHIMPS sample. The much larger CHIMPS sample is illustrated as a 2D hexagonal histogram to allow the point density to be seen more easily. In all cases, we find that the relationship between R_σ and $R_{\rm eq}$ is well fitted by a power law. We performed a power-law fit to the two radii types for each sample using an orthogonal distance regression[5] to account for the uncertainties on both variables. The fit results are reported in Table 5. We find that the `fwhires` and `fwlores` source extractions produce essentially identical relationships, with power-law indices of 0.66 ± 0.01 and 0.69 ± 0.03, respectively. This is unsurprising because the two extractions are very similar, differing only in the level of fragmentation that they allow (`fwhires` structures exist within `fwlores` structures).

The relationship between the two radius types for the `fwchimps` and the Inner Galaxy samples are also non-linear and with power-law indices of 0.81 ± 0.03 and 0.85 ± 0.01, respectively, and are consistent with each other. This suggests that there are no significant differences in the mean emission profile for sources at Galactocentric distances of 9–10 kpc compared with sources at 5–7 kpc.

The difference between the fit to the `fwchimps` data and the `fwlores` and `fwhires` is caused by the differences in data quality and to the FELLWALKER parameter setup, which we have modified in PAMS compared with CHIMPS. We note that some of the non-fitted points in Figs 9(a) and (b) show unusually high or low values of η_R. In cases where R_σ is much larger than $R_{\rm eq}$, these are the archipelago sources that FELLWALKER identifies at low SNR. The sources with much larger $R_{\rm eq}$ than R_σ look like well-recovered sources that are diffuse and have flat emission profiles, and these are overrepresented in the data due to a selection bias in FELLWALKER; the requirement

[5]Using `scipy.odr`.

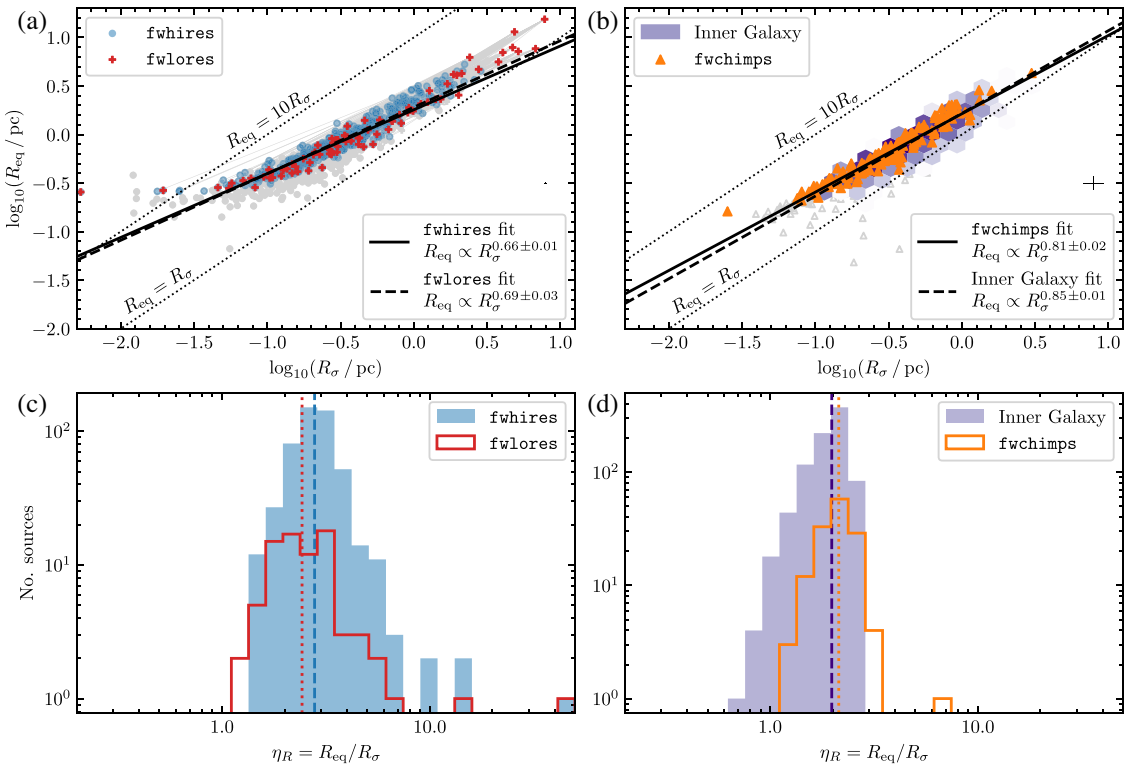

Figure 9. Comparison of intensity-weighted rms radii R_σ and equivalent radii R_{eq} for sources extracted from PAMS and the $2 \geq d \leq 4$ kpc Inner Galaxy sample for CHIMPS. (a) Comparison between radii derived from the `fwhires` and `fwlores`FELLWALKER extractions. Where a `fwhires` source is a fragment of a larger source in the `fwlores` extraction, it is linked to its parent with a grey line. (b) Comparison of radii from the `fwchimps`FELLWALKER PAMS source extraction, (orange triangles), and the CHIMPS Inner Galaxy sample (hexagonal histogram). The colours of the hexagonal histogram data have been normalized with a logarithmic intensity scaling. In Panels (a) and (b) the solid and dashed lines show the best-fitting power-law relationships, and we show the points not used in the fit (with peak SNR < 9) as empty grey symbols. Median error bars are indicated to the right. Panels (c) and (d) show the distributions of η_R for the points used in the fits in Panels (a) and (b), respectively, with median values indicated by dashed and dotted vertical lines for the filled and empty histograms, respectively.

Table 5. The results of fitting to the relationships described in Sections 4.2.1 and 4.2.2. The fits were made in log space, where $\log_{10}(y) = m \log_{10}(x) + \log_{10}(k)$ for a relationship $y = kx^m$. Uncertainties from the fitting algorithm on m and $\log_{10}(k)$ are also provided.

Sample	x	y	$\log_{10}(k)$	$\Delta \log_{10}(k)$	m	Δm
`fwhires`	R_σ/pc	R_{eq}/pc	0.255	0.007	0.657	0.010
`fwlores`	R_σ/pc	R_{eq}/pc	0.281	0.019	0.685	0.025
`fwchimps`	R_σ/pc	R_{eq}/pc	0.214	0.012	0.807	0.020
Inner Galaxy	R_σ/pc	R_{eq}/pc	0.218	0.005	0.852	0.011
`fwhires`	R_σ/pc	Δv/km s^{-1}	0.080	0.016	0.284	0.027
`fwlores`	R_σ/pc	Δv/km s^{-1}	0.040	0.020	0.405	0.033
`fwchimps`	R_σ/pc	Δv/km s^{-1}	0.121	0.026	0.437	0.052
Inner Galaxy	R_σ/pc	Δv/km s^{-1}	0.142	0.010	0.478	0.024
`fwhires`	R_σ/pc	$M/M_\odot$	3.558	0.036	2.010	0.057
`fwlores`	R_σ/pc	$M/M_\odot$	3.252	0.055	1.779	0.081
`fwchimps`	R_σ/pc	$M/M_\odot$	3.824	0.055	2.146	0.096
Inner Galaxy	R_σ/pc	$M/M_\odot$	3.511	0.029	2.490	0.067

for sources to have a minimum number of pixels above the intensity defined as the noise level prefers diffuse over compact sources. Such sources are also more likely to be the beneficiary of flux boosting effects, in which positive contributions to the emission from the noise may be represented in the data, but negative contributions will not.

Rigby et al. (2019) reported a median value of $\eta_R = 2.0$ across the full CHIMPS sample, and the same value for our distance-limited Inner Galaxy sample (Fig. 9d). For `fwchimps`, the figure is slightly larger at 2.1. By contrast, the `fwhires` and `fwlores` median η_R values are larger at 2.8 and 2.4, respectively, which is expected for more-sensitive data. Overall, the emission profiles of the PAMS sources are similar to those of the Inner Galaxy sample, suggesting that any differences in emission characteristics between 5–7 and 9–10 kpc are mild.

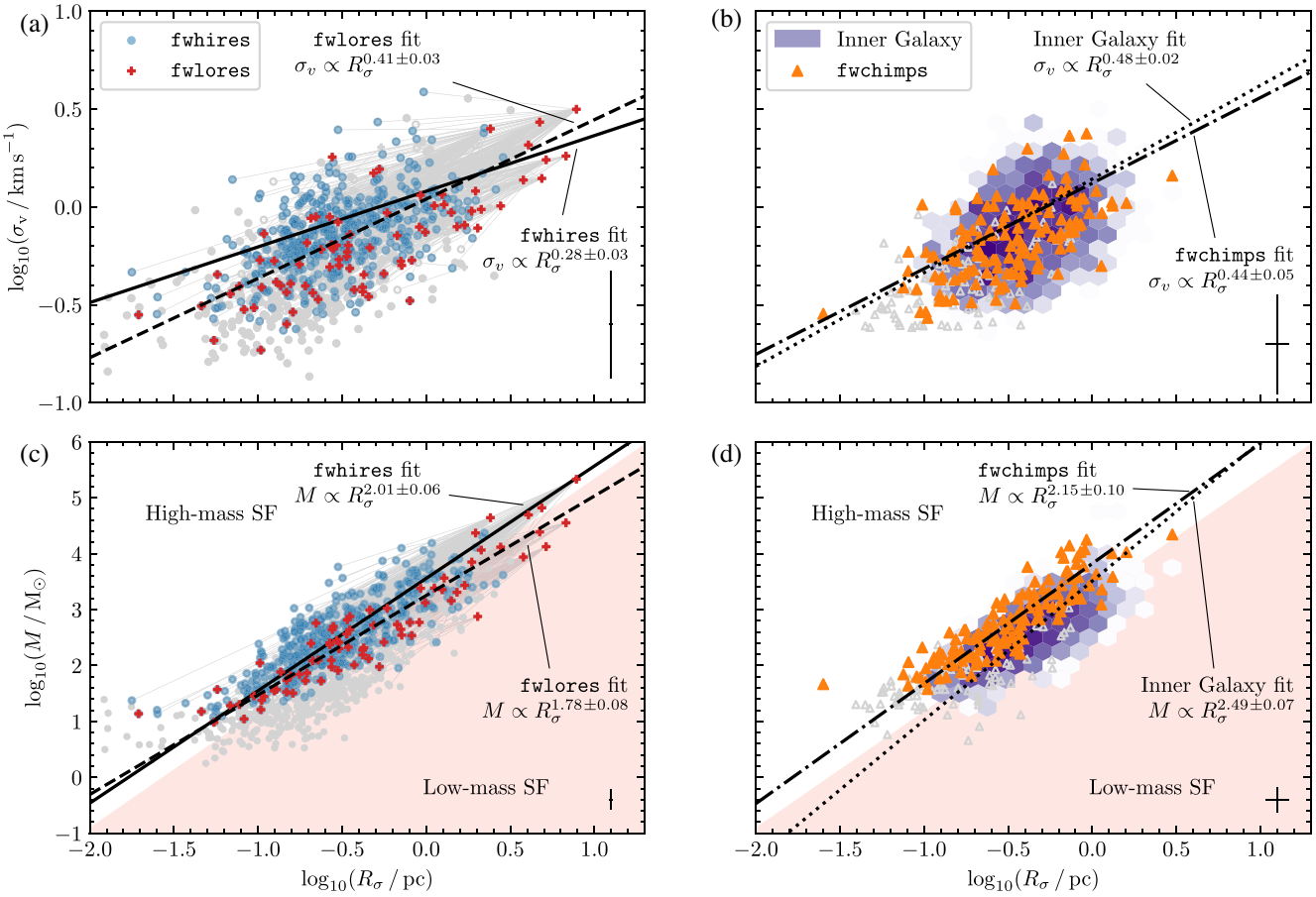

Figure 10. *Top row*: Size–linewidth relationships for PAMS and CHIMPS sources. *Bottom row*: Mass–radius relationships for PAMS and CHIMPS clumps. For both rows, the figures in the left column show the distribution of points from the `fwhires` and `fwlores` extractions, along with their lines of best fit. The figures in the right column show the distribution of sources from CHIMPS as hexagonal 2D histograms, and the `fwchimps` PAMS extraction as triangles. The darkness of the hexagonal histogram data have been normalized with a logarithmic intensity scaling. The shaded area denotes the region that has been empirically found to be devoid of high-mass star formation in local star-forming regions (adapted from Kauffmann & Pillai 2010). Median error bars are shown to the lower right in each panel. Points not used in the fitting have smaller lighter markers.

4.2.2 *Scaling relationships*

Fig. 10 shows the size–linewidth and mass–radius relationships for different samples of our PAMS data, and with a comparison to the same distance-limited Inner Galaxy sample as in the previous section. We also explored the differences in cloud properties that might arise from our different observations and FELLWALKER parameter settings by showing the relationships for each of the `fwhires`, `fwlores`, and `fwchimps` extractions. Masses were derived according to:

$$M = \mu_{\mathrm{H_2}} m_{\mathrm{H}} d^2 X_{^{13}\mathrm{CO}\,3-2} \int W(^{13}\mathrm{CO}\,3-2)\,\mathrm{d}\Omega, \qquad (10)$$

where $\mu_{\mathrm{H_2}}$ is the molecular weight per hydrogen molecule, with a value of 2.8 (accounting for a 71 per cent abundance of hydrogen, 27 per cent helium, and 2 per cent metals), m_{H} is the mass of a hydrogen atom, d is the source distance, $X_{^{13}\mathrm{CO}\,3-2}$ is the X-factor calculated for ^{13}CO (3–2) derived in Section 4.1, $W(^{13}\mathrm{CO}\,3-2)$ is the integrated intensity of ^{13}CO (3–2) per pixel, and dΩ is the angular area of a pixel. We adopted the Method (i) values of $X_{^{13}\mathrm{CO}\,(3-2)} = 4.8 \times 10^{21}$ and $2.4 \times 10^{21}\,\mathrm{cm^{-2}\,(K\,km\,s^{-1})^{-1}}$ as our best overall estimate for resolved regions in the Inner and Outer Galaxy samples (i.e. CHIMPS and PAMS), respectively, with a factor of 1.5 uncertainty. We note that although Rigby et al. (2019) calculated clump masses for the CHIMPS sources using an LTE analysis, we apply the same X_{CO} derivation here for consistency with the PAMS data. We will calculate the masses of PAMS sources using LTE analysis for a comparison with the CHIMPS LTE masses and excitation conditions in a future paper.

We fitted power laws to the size–linewidth and mass–radius relationships using orthogonal distance regression, as in Section 4.2.1, and present the results in Table 5. Fig. 10(a) shows that the size–linewidth relationships[6] for the `fwlores` and `fwhires` extractions show similar relationships, considering the uncertainties. Although `fwlores` has a slightly steeper relationship, for the most part, the `fwhires` sources have higher linewidths for a given size. This is a result of the greater level of fragmentation allowed in the `fwhires`

[6]For the uncertainty on the linewidth, we use the difference between the measured linewidth and the *corrected linewidth* that depends on the peak SNR of the source, which is given by $\sigma_v^* = \sigma_v(13.3/(\mathrm{SNR}+5.5)$. This empirical relationship was reported in equation (8) of Rigby et al. (2019), and accounts for the clipping of the linewidth caused by the detection thresholds used by FELLWALKER (and any other source-extraction algorithms that do not explicitly model emission profiles, e.g. dendrograms), though the correction factor was erroneously described as the uncertainty itself.

extraction, where larger linewidths are recovered due to intracloud variations that are averaged out in the corresponding `fwlores` extraction. This is illustrated by the lines connecting the `fwhires` sources to their `fwlores` parent. For example, the NGC 7538 region catalogues contain 58 and 132 entries in the `fwlores` and `fwhires` extractions, respectively, but the bulk of the mass (95 per cent of the ^{13}CO emission) is recovered as a single source in the `fwlores` catalogue, which is the parent structure of 73 of the sources (i.e. around half) featuring in the `fwhires` catalogue. The size–linewidth relationships for the `fwchimps` and CHIMPS Inner Galaxy samples are almost identical.

The mass–radius relationships show more significant differences. Comparing the `fwlores` and `fwhires` source extractions, the `fwhires` sources have a steeper power-law index of 2.01 compared with 1.78 to `fwlores`, but again the difference is not significantly different when considering the uncertainties. The weak differences in the distributions correspond to a scale dependence in the density distributions of the sources; we note the greater frequency of clump-scale substructures – with sizes of $\lesssim 3$ pc and masses of $\lesssim 10,000\,\mathrm{M}_\odot$ – in the `fwhires` distribution. When comparing the `fwchimps` and Inner Galaxy samples, the power-law index is steeper in the Inner Galaxy compared with the Outer Galaxy, with a value of 2.49 for CHIMPS compared with 2.16 for PAMS, but they are consistent within the uncertainties. This consistency indicates that the mean density profile of sources in the two samples are similar.

In Fig. 10, we also illustrate the relationship of Kauffmann & Pillai (2010) that delineates the parameter space that is empirically found to be devoid of high-mass star formation (HMSF) in nearby clouds. The original relationship was devised in terms of $R_{\rm eq}$, with $m(r) \leq 870\,M_\odot (R_{\rm eq}/\mathrm{pc})^{1.33}$ as the limit. Since we have favoured R_σ, the relationship requires modification for application to our data, and we adopt $R_{\rm eq} = 1.75 R_\sigma^{0.75}$ – as the average of the fitted parameters in Section 4.2.1 – and our adapted relationship is therefore $m(r) \leq 1830\,M_\odot (R_{\rm eq}/\mathrm{pc})^{2.08}$. The majority of sources in the samples fitted in Fig. 10 are capable of forming high-mass stars, with 79 and 61 per cent for the fitted `fwhires` and `fwlores` samples, respectively. The proportion appears to be higher, in fact, than is the case for the CHIMPS survey, with 96 and 63 per cent of the sources from the fitted CHIMPS and `fwchimps` samples, respectively, satisfying the condition. We will explore why this might be the case in Section 5 for HMSF.

4.3 Galactocentric dependence

The combination of PAMS and CHIMPS allows for an expanded study of properties as a function of Galactocentric distance. The longitude coverage of CHIMPS means that the only clouds in the survey that lie outside the solar circle are at the far side of the Galaxy, with distances in the range ∼12–17 kpc. Consequently, those clouds are both few in number, and sample only the extreme high-column-density (and therefore high-mass) end of the underlying distributions due to Malmquist bias. The PAMS data therefore make an important contribution to Galactocentric trends by significantly improving the population statistics at $D_{\rm GC}$ ∼9–10 kpc, with much improved spatial resolution.

In Fig. 11(a) we display the mass distributions from CHIMPS (greyscale hexagonal histogram) and PAMS (blue hexagonal histogram). For both PAMS and CHIMPS, we take the masses calculated from our $X_{^{13}\mathrm{CO}\,(3-2)}$ factor from Section 4.1. We determined mean radial trends on a subsample of the data by first excluding all sources with peak SNRs of less than 9, as in Sections 4.2.1 and 4.2.2, and applying the mass-completeness threshold derived by Rigby et al. (2019, their equation B.1) – shown as the red dashed line – removing all sources at $d > 12$ kpc, and all sources with $M < 1250\,\mathrm{M}_\odot$. The completeness threshold should remove some of the effects of Malmquist bias. The solid orange line in Fig. 11 shows the moving average value of $\log_{10}(M/\mathrm{M}_\odot)$, with a window size of 0.1 kpc, to all sources in the subsample. It is apparent that the PAMS clumps are consistent with their Inner Galaxy counterparts, and we do not see any systematic trends over the range of $R_{\rm GC}$ probed. This is not affected by the different FELLWALKER parameter configurations. As far as we can tell with these data, the cloud-mass distributions in ^{13}CO (3–2) do not vary with Galactocentric distance.

In Section 4.2.2, we found slight differences in the power-law index of the mass–radius relationship between PAMS and CHIMPS clouds, indicating that the two populations may have slightly different density profiles. We therefore examine the distribution of average volume densities in Fig. 11(b), calculated by:

$$n(\mathrm{H_2}) = \frac{3}{4\pi}\frac{M}{\mu_{\mathrm{H_2}} m_{\mathrm{H}} R_{\rm eq}^3}. \tag{11}$$

Here we adopt the equivalent radius to ensure that the mass and radius are calculated for the same volume. We calculated average Galactic radial profiles using the same reduced sample above containing only sources satisfying the minimum mass and SNR criteria, which are, again, shown in orange. The distribution of PAMS densities for the `fwhires` extraction is consistent with the Inner Galaxy, whereas for `fwlores` the mean values are a factor of ∼2 lower. The latter extraction suppresses small-scale structure, and so reports cloud complexes that evidently have lower mean densities (when using $R_{\rm eq}$ for the calculation) due to the extended low-column-density envelopes that PAMS is more sensitive to. We therefore caution here that comparing distributions such as these derived from different source–extraction methods will almost certainly result in differences. When we compare like-for-like extractions, the PAMS densities within the `fwchimps` distribution are a factor of ∼4 higher than their CHIMPS counterparts, which is somewhat surprising, and we see the same offset when considering the binned radial trend. This is explainable as a distance-related bias: In the CHIMPS sample, the relationship between Galactocentric and heliocentric distances bifurcates (see fig. 12g of Rigby et al. 2019) due to the overlapping of sources in the near and far sides of the Galactic disc in velocity. This bifurcation is visible in the distribution of mean densities in Fig. 11(b) at $R_{\rm GC} \approx 8$ kpc, with sources at the far distance occupying the lower density branch and vice versa for sources at the near distance. This explains this apparent trend. In the lower right panel we demonstrate this by plotting a secondary radial trend where we limited the CHIMPS sample to sources within the same 2–4 kpc distance range that we have in our PAMS sample, and it is clear that the radial trend is consistent with that of the `fwchimps` extraction of PAMS. The mean densities are particularly sensitive to distance effects when using a clump-scale extraction, with more internal substructures being discernible in closer sources. Extraction techniques which prefer to recover the largest scale structures such as `fwlores`, or SCIMES (e.g Colombo et al. 2015, 2019; Duarte-Cabral et al. 2021; Rani et al. 2022) are therefore more suitable for examining Galactocentric gradients.

5 DISCUSSION

5.1 Galactocentric gradients in $X_{\rm CO}$

In Section 4.1, we calculated $X_{\rm CO}$ factors for ^{12}CO and ^{13}CO (3–2) between the Inner and Outer Galaxy by comparing *Herschel*-derived

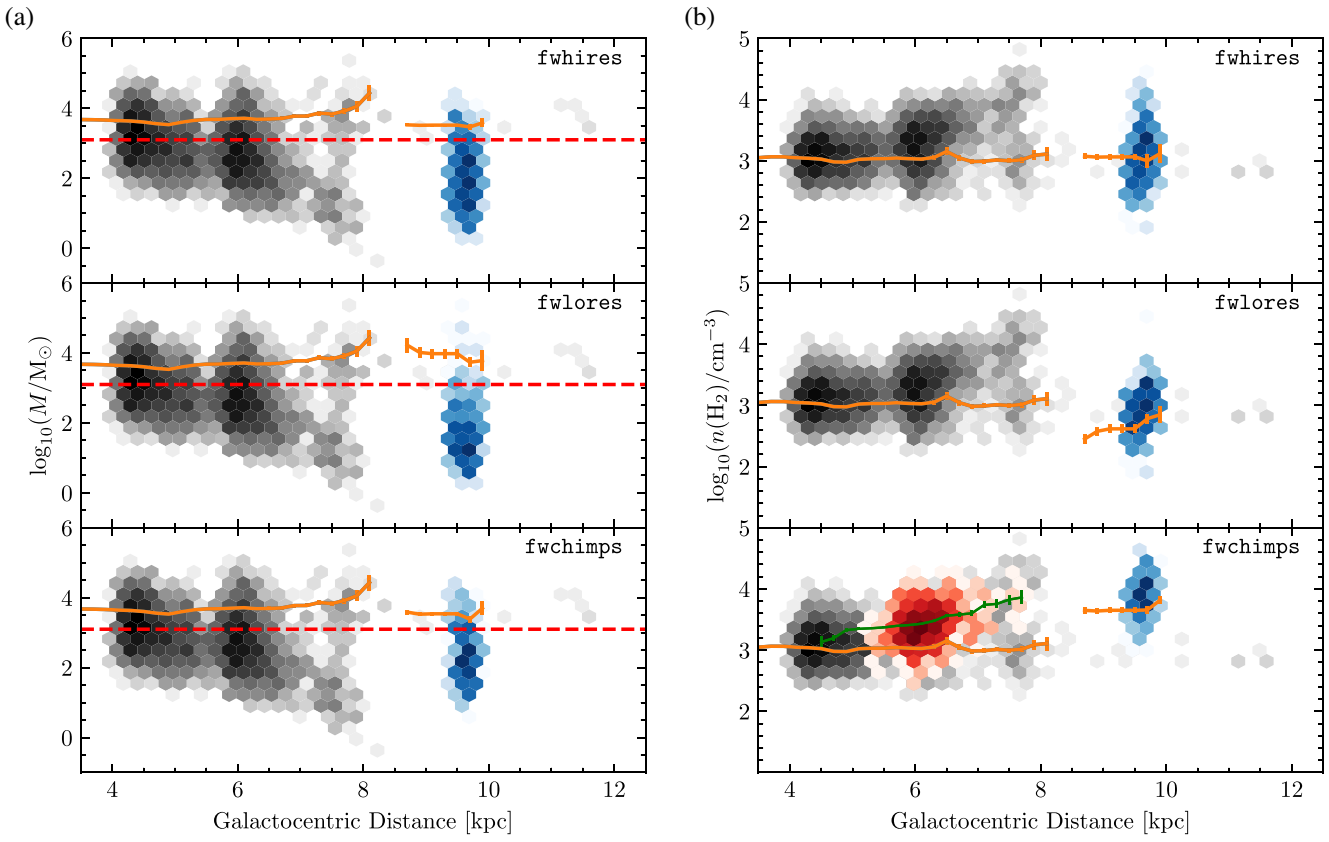

Figure 11. Logarithm of mass (*left column*) and density (*right column*) as a function of Galactocentric distance for clouds within CHIMPS (greyscale histogram Rigby et al. 2019), and PAMS (blue histogram; this paper), for the `fwhires`, `fwlores`, and `fwchimps` extractions from PAMS, respectively. The dashed line indicates the sample mass-completeness limit, adapted from the CHIMPS calculation. The solid lines indicate the moving average in 0.2-kpc-wide bins for clouds that satisfy the mass-completeness limit. The lower-right panel also highlights CHIMPS data in the distance range 2–4 kpc, with a secondary radial trend indicated by the thin line.

H_2 column densities with data from the COHRS (Dempsey et al. 2013; Park et al. 2023), CHIMPS (Rigby et al. 2016), and PAMS data, summarizing the results in Tables 3 and 4. The Inner Galaxy sightline used was at $\ell = 30°$, whose emission is dominated by the W43 star-forming region at a distance of 5.2 kpc (Urquhart et al. 2018), corresponding to a Galactocentric radius of $R_{GC} = 4.5$ kpc. We assume that our Inner Galaxy X-factors are weighted somewhere slightly closer along the line of sight than W43, so we will take $R_{GC} =$ 5.0 kpc as the representative value for the Inner Galaxy results,[7] while the PAMS regions are located close to $R_{GC} = 9.5$ kpc.

We found that the distributions of $X_{^{12}CO\,(3-2)}$ and $X_{^{13}CO\,(3-2)}$ values calculated on a pixel-by-pixel basis were significantly different between the Inner and Outer Galaxy regions (and this is confirmed by both Kolmogorov–Smirnov and Anderson–Darling statistical tests). For ^{12}CO, the difference is relatively small. Our suggested global value of $X_{^{12}CO\,(3-2)} = 4.0 \times 10^{20}\,cm^{-2}\,(K\,km\ s^{-1})^{-1}$ is weighted towards the Inner Galaxy value, and is identical to the value adopted by Colombo et al. (2019) who also used COHRS data. If one considers a common formulation of

$$X_{^{12}CO(3-2)} = \frac{X_{^{12}CO(1-0)}}{R_{31}}, \tag{12}$$

where R_{31} is the ^{12}CO (3–2)/(1–0) line ratio, these results imply an average value of $R_{31} = 0.5$, which is consistent with observations of nearby galaxies (e.g. Lamperti et al. 2020), high-redshift galaxies (e.g. Aravena et al. 2014) and simulations (e.g. Peñaloza et al. 2018). The Inner and Outer Galaxy distributions of $X_{^{12}CO\,(3-2)}$ values in Fig. 7 overlap substantially, and representative values for the Outer Galaxy tend to be a factor of 1.3–2.0 lower than their Inner Galaxy counterparts (see Table 3). Taking equation (12) literally, these results would imply that R_{31} increases with Galactocentric distance, from ∼0.5 to 0.7 between 5.0 and 9.5 kpc based on equation (refeq:R31). This is contrary to the shallow gradients in R_{21} (which we assume would hold the same trend) found by Sakamoto et al. (1997) in the Milky Way and Den Brok et al. (2022) in M51, but this implication would only hold if the values of $X_{^{12}CO\,(3-2)}$ and X_{CO} do not vary at the same time. Since we are not directly probing the intensity ratio here, other factors may affect this result.

In equation (4) in Section 4.1 we used a single value of $\gamma = 100$ for the gas-to-dust mass ratio, which was shown by Giannetti et al. (2017) to have a Galactocentric dependence (with a large scatter). The Galactic gradient presented in that study would imply a variation of $\gamma = 75$ to 185 between R_{GC} =5.0 to 9.5 kpc, and such a variation could reverse the apparent increasing trend in R_{31} to a decreasing one, and simultaneously reduce the magnitude of the trend. Rescaling the Inner and Outer Galaxy X_{CO} values based on this γ gradient would result in $X_{^{12}CO\,(3-2)} \approx 3.0 \times 10^{20}$

[7]The intensity-weighted Galactocentric radius from the Rigby et al. (2019) catalogue of clumps in the longitude range of the tile gives a compatible result.

and 4.5×10^{20} cm^{-2} (K km s^{-1})$^{-1}$ for the Inner and Outer Galaxy, respectively, implying R_{31} decreasing from ∼0.65 to 0.45 over the same range. For ^{13}CO (3–2), the trend also reverses, resulting in $X_{^{13}\mathrm{CO}\,(3-2)} \approx 3.6 \times 10^{21}$ and 4.4×10^{21} cm^{-2} (K km s^{-1})$^{-1}$ for the Inner and Outer Galaxy, respectively. Considering this variation, a value of 4.0×10^{21} cm^{-2} (K km s^{-1})$^{-1}$ is appropriate for general use in the Galactic disc for sources lying within ∼4–10 kpc of the Galactic Centre, and incorporates the γ gradient. A factor of 1.5 uncertainty encapsulates much of the variation we have seen.

Our Inner and Outer Galaxy values of $X_{^{12}\mathrm{CO}\,(3-2)}$ and $X_{^{13}\mathrm{CO}\,(3-2)}$ do not vary significantly, given the uncertainties in the gas-to-dust mass ratio, and our results are not inconsistent with a radially decreasing R_{31}. More-robust direct measurements of R_{31} could be obtained in future at ∼50-arcsec resolution using the MWISP data, or at ∼20-arcsec resolution using a combination of CHIMPS, PAMS, COHRS, and FUGIN data.

In all cases, the relationship between H_2 column density and integrated intensity of ^{12}CO and ^{13}CO (3–2) emission is, of course, more complex than a simple multiplicative factor as can clearly be seen in Fig. 8 Panels (a) and (d). Barnes et al. (2015) remarked on similar behaviour for ^{12}CO (1–0) emission and suggested adopting a power-law relationship for the column density of CO where $N(\mathrm{CO}) \propto W(^{12}\mathrm{CO}\,1{-}0)^{1.38}$, however, the relationships that we report are clearly also not linear in log-space, indicating that even a single power law would not accurately reproduce the behaviour. A power law with an index of > 1 would help reproduce the superlinear parts of the distributions in Figs 8(a) and (d), but these would then underpredict $N(H_2)$ at low CO intensity. Our Method (ii) values that incorporate a background column density could help alleviate this issue, but we cannot be certain whether the background column density is a result of the greater column of Galactic disc that the Inner Galaxy sightline contains, or if it is reflective of a difference in excitation conditions of CO; subthermal emission of CO would also cause an flattening of the relationship at low CO intensity. We therefore recommend that the single representative X_{CO} values should be used in the knowledge that more-accurate column densities may be determined through LTE modelling of the combination of ^{12}CO, ^{13}CO, and – where available – C^{18}O emission in combination.

5.2 Galactocentric gradients in molecular-cloud properties

In Section 4.2, we compared the properties of sources extracted from PAMS with those from a different Inner Galaxy sample from CHIMPS. Here, we created a distance-limited sample of CHIMPS clouds with distances between 2 and 4 kpc – approximately matching the PAMS range of distances – corresponding to Galactocentric radii of 5–7 kpc. In Fig. 9 we found no substantial differences between two types of radius measurement between the two samples, when considering the `fwchimps` sources extraction that was designed to replicate the CHIMPS setup as closely as possible, indicating that the emission profiles of sources in the two samples are similar. The size–linewidth and mass–radius relationships of the two samples of extracted sources in Fig. 10 were again found to be consistent.

One notable difference is that the masses of PAMS sources tend to be greater for a given size-scale (Fig. 10), with difference between the distributions of $\log_{10}(M/\mathrm{M}_\odot)$ of ∼0.15 dex (i.e. around 40 per cent). A surprising result follows, which is that a greater proportion of the PAMS sample satisfy the Kauffmann & Pillai (2010) criterion for HMSF than for CHIMPS, with 96 and 63 per cent of the fitted samples doing so, respectively. At face value, this would suggest that the molecular clouds at $R_{\mathrm{GC}} = 9.5$ kpc have more massive star-forming potential than those at $R_{\mathrm{GC}} \sim 6.0$ kpc, which is contrary to our expectations, e.g. the decreasing fraction of star-forming Hi-GAL clumps reported by Ragan et al. (2016). Since the `fwchimps` source extraction accounts for the differences in data quality between PAMS and CHIMPS, we can rule out biases arising from differences in sensitivity. This discrepancy is made worse if we account for the Galactic gradient in the gas-to-dust mass ratio γ, discussed in the previous section, which would suggest that our Inner and Outer Galaxy $X_{^{13}\mathrm{CO}\,(3-2)}$ factors were over- and underestimated, respectively. On the other hand, Giannetti et al. (2017) point to large uncertainties on γ for individual star-forming regions, as well as intrinsic scatter, and so this may partly be a result of the small number of independent star-forming complexes that PAMS covers. Additionally, while the Outer Galaxy $X_{^{13}\mathrm{CO}\,(3-2)}$ values derived in Section 4.1 for the various methods varied little, the Inner Galaxy values were wider-ranging, and the Method (iii) value is ∼50 per cent larger than the Method (i) value we adopted, and this may account for another part of the discrepancy. Furthermore, selection biases resulting from the PAMS survey being targeted towards well-known star-forming regions (in contrast to the blind survey mode of CHIMPS) may account for a further part of the discrepancy. While we can find no single explanation that is entirely satisfactory, we suggest a combination of the above factors may explain this result. Overall, we do not find any significant differences between the sources in the Inner and Outer Galaxy over $5 \leq R_{\mathrm{GC}} \leq 10$ kpc.

6 CONCLUSIONS

We have presented the PAMS, a survey of ^{12}CO, ^{13}CO, and C^{18}O (3–2), covering ∼8 deg^2 over several molecular-cloud complexes in the Outer Galaxy, at Galactocentric radii of ∼9.5 kpc. In Section 4.1, we calculated X_{CO} factors for ^{12}CO and ^{13}CO (3–2), which convert the integrated intensity of the CO emission into molecular-hydrogen column density, and examined the distributions of pixel values. In Section 4.2, we compared basic properties of sources extracted from PAMS with equivalent values from the CHIMPS survey in order to probe any differences between these Inner and Outer Galaxy environments, covering a range of Galactocentric radii between 4 and 10 kpc.

Our main findings are as follows:

(i) The systematic variation in X_{CO} values derived for the Inner and Outer Galaxy were generally small compared with the variation arising from the different methods, as well as the spread in individual pixel values, but that difference was stronger in ^{13}CO (3–2) than ^{12}CO (3–2).

(ii) We recommend the usage of a value of $X_{^{12}\mathrm{CO}\,(3-2)} = 4.0 \times 10^{20}$ cm^{-2} (K km s^{-1})$^{-1}$ to convert ^{12}CO (3–2) integrated intensity to molecular-hydrogen column density, with a factor of 1.5 uncertainty, in agreement with previous studies (e.g. Colombo et al. 2019).

(iii) For ^{13}CO (3–2), we recommend the usage of a value of $X_{^{13}\mathrm{CO}\,(3-2)} = 4.0 \times 10^{21}$ cm^{-2} (K km s^{-1})$^{-1}$ to convert ^{13}CO (3–2) integrated intensity to molecular-hydrogen column density, with a factor of 1.5 uncertainty.

(iv) Although the $X_{^{13}\mathrm{CO}\,(3-2)}$ values we recovered are significantly different for the Inner and Outer Galaxy (traced by CHIMPS and PAMS), with $X_{^{13}\mathrm{CO}\,(3-2)} = 4.8 \times 10^{21}$ cm^{-2} (K km s^{-1})$^{-1}$ for the Inner Galaxy and 2.4×10^{21} cm^{-2} (K km s^{-1})$^{-1}$ for the Outer Galaxy, accounting for the Galactic gradient in gas-to-dust mass ratio can resolve much of the difference. Calculating H_2 column densities from LTE analysis of cospatial ^{12}CO and ^{13}CO emission would be preferable to relying on X_{CO} factors.

(v) We did not find any significant differences between the emission profiles, of sources extracted from the ^{13}CO (3–2) PAMS data at Galactocentric distances of 9–10 kpc and from an equivalent sample of sources extracted from CHIMPS ^{13}CO (3–2) data at Galactocentric distances of 5–7 kpc. Similarly, the size–linewidth and mass–radius relationships were also compatible.

(vi) Although the distributions of masses of PAMS Outer Galaxy sources are shifted to greater values than their CHIMPS Inner Galaxy counterparts for a given size scale, most of the ∼0.2 dex difference can be explained by a combination of variations in gas-to-dust mass ratios and selection biases.

Finally, we have demonstrated that the PAMS data are a valuable addition to the existing repertoire of publicly available ^{12}CO, ^{13}CO, and C^{18}O (3–2) survey data in the Outer Galaxy. In combination with surveys such as CHIMPS, CHIMPS2, and COHRS, these data extend the baseline in Galactocentric radius in what can be studied in the 3–2 rotational transition across different Galactic environments, in addition to the growing number of surveys covering 2–1 and 1–0.

ACKNOWLEDGEMENTS

We would like to thank the anonymous referee whose review helped us to improve the quality and accuracy of the manuscript. We thank Andrea Giannetti for a thoughtful discussion about gas-to-dust mass ratios. AJR acknowledges postdoctoral support from the University of Leeds. The JCMT is operated by the East Asian Observatory on behalf of The National Astronomical Observatory of Japan; Academia Sinica Institute of Astronomy and Astrophysics; the Korea Astronomy and Space Science Institute; the National Astronomical Research Institute of Thailand; Center for Astronomical Mega-Science (as well as the National Key R&D Programme of China with No. 2017YFA0402700). Additional funding support is provided by the Science and Technology Facilities Council of the United Kingdom and participating universities and organizations in the United Kingdom and Canada. The JCMT has historically been operated by the Joint Astronomy Centre on behalf of the Science and Technology Facilities Council of the United Kingdom, the National Research Council of Canada and the Netherlands Organisation for Scientific Research. The authors wish to recognize and acknowledge the very significant cultural role and reverence that the summit of Maunakea has always had within the indigenous Hawaiian community. We are most fortunate to have the opportunity to conduct observations from this mountain. This research used the facilities of the Canadian Astronomy Data Centre operated by the National Research Council of Canada with the support of the Canadian Space Agency. This research has made use of NASA's Astrophysics Data System Bibliographic Services'.

Software: Python packages: `astropy` (The Astropy Collaboration 2022), `ipython` (Perez & Granger 2007), `matplotlib` (Hunter 2007), `multicolorfits` (Cigan 2019), `numpy` (Harris et al. 2020), `scipy` (Virtanen et al. 2020), `scikit-learn` (Pedregosa et al. 2011).

Starlink (Currie et al. 2014) applications: `gaia`, `kappa` (Currie & Berry 2013), `cupid/fellwalker` (Berry 2015), `orac-dr` (Jenness et al. 2015).

Other software: `topcat` (Taylor 2005).

DATA AVAILABILITY

We make the PAMS data publicly available at https://dx.doi.org/10.11570/25.0001. This repository includes the ^{12}CO, ^{13}CO, and C^{18}O (3–2) mosaics of each region, and the FELLWALKER catalogues with their corresponding assignment masks.

REFERENCES

Aravena M. et al., 2014, MNRAS, 442, 558
Barnes P. J., Muller E., Indermuehle B., O'Dougherty S. N., Lowe V., Cunningham M., Hernandez A. K., Fuller G. A., 2015, ApJ, 812, 6
Barnes A. T., Longmore S. N., Battersby C., Bally J., Kruijssen J. M. D., Henshaw J. D., Walker D. L., 2017, MNRAS, 469, 2263
Benedettini M. et al., 2020, A&A, 633, A147
Benjamin R. A. et al., 2003, PASJ, 115, 953
Berry D. S., 2015, Astron. Comput., 10, 22
Berry D. S., Reinhold K., Jenness T., Economou F., 2007, in Shaw R. A., Hill F., Bell D. J., eds, ASP Conf. Ser. Vol. 376, Astronomical Data Analysis Software and Systems XVI. Astron. Soc. Pac. , San Francisco, p. 425
Bolatto A. D., Wolfire M., Leroy A. K., 2013, ARA&A, 51, 207
Buckle J. V. et al., 2009, MNRAS, 399, 1026
Chapin E., Gibb A. G., Jenness T., Berry D. S., Scott D., Tilanus R. P. J., 2013, Starlink User Note, 258
Cigan P., 2019, Astrophysics Source Code Library. record ascl:1909.002
Clarke J. P., Gerhard O., 2022, MNRAS, 512, 2171
Colombo D., Rosolowsky E., Ginsburg A., Duarte-Cabral A., Hughes A., 2015, MNRAS, 454, 2067
Colombo D. et al., 2019, MNRAS, 483, 4291
Colombo D. et al., 2022, A&A, 658, A54
Currie M. J., Berry D. S., 2013, Starlink User Note, 95
Currie M. J., Berry D. S., Jenness T., Gibb A. G., Bell G. S., Draper P. W., 2014, in Manset N., Forshay P., eds, ASP Conf. Ser. Vol. 485, Astronomical Data Analysis Software and Systems XXIII. Astron. Soc. Pac., San Francisco, p. 391
Dempsey J. T., Thomas H. S., Currie M. J., 2013, ApJS, 209, 8
Den Brok J. S. et al., 2022, A&A, 662, A89
Duarte-Cabral A. et al., 2021, MNRAS, 500, 3027
Eden D. J., Moore T. J. T., Morgan L. K., Thompson M. A., Urquhart J. S., 2013, MNRAS, 431, 1587
Eden D. J., Moore T. J. T., Urquhart J. S., Elia D., Plume R., Rigby A. J., Thompson M. A., 2015, MNRAS, 452, 289
Eden D. J. et al., 2020, MNRAS, 498, 5936
Fallscheer C. et al., 2013, ApJ, 773, 102
Federrath C. et al., 2016, ApJ, 832, 143
Frerking M. A., Langer W. D., Wilson R. W., 1982, ApJ, 262, 590
Giannetti A. et al., 2017, A&A, 606, L12
Ginsburg A., Bally J., Williams J. P., 2011, MNRAS, 418, 2121
Goldsmith P. F., 2001, ApJ, 557, 736
Harris C. R. et al., 2020, Nature, 585, 357
Heyer M. H., Brunt C., Snell R. L., Howe J. E., Schloerb F. P., Carpenter J. M., 1998, ApJSS, 115, 241
Hunter J. D., 2007, Comput. Sci. Eng., 9, 90
Jackson J. M. et al., 2006, ApJSS, 163, 145
Jenness T., Currie M. J., Tilanus R. P. J., Cavanagh B., Berry D. S., Leech J., Rizzi L., 2015, MNRAS, 453, 73
Kauffmann J., Pillai T., 2010, ApJ, 723, L7
Kauffmann J., Pillai T., Shetty R., Myers P. C., Goodman A. A., 2010, ApJ, 712, 1137
Kauffmann J., Pillai T., Zhang Q., Menten K. M., Goldsmith P. F., Lu X., Guzmán A. E., 2017, A&A, 603, A89
Kutner M. L., Ulich B. L., 1981, ApJ, 250, 341
Lamperti I. et al., 2020, ApJ, 889, 103
Larson R. B., 1981, MNRAS, 194, 809
Longmore S. N. et al., 2013, MNRAS, 429, 987
Luck R. E., Lambert D. L., 2011, ApJ, 142, 136
Marsh K. A. et al., 2017, MNRAS, 471, 2730
Maud L. T., Moore T. J. T., Lumsden S. L., Mottram J. C., Urquhart J. S., Hoare M. G., 2015, MNRAS, 453, 645
Molinari S. et al., 2016, A&A, 591, A149

Moore T. J. T., Urquhart J. S., Morgan L. K., Thompson M. A., 2012, MNRAS, 426, 701
Motte F. et al., 2010, A&A, 518, L77
Nettke W. et al., 2017, MNRAS, 468, 250
Ossenkopf V., Henning Th., 1994, A&A, 291, 943
Park G. et al., 2023, ApJS, 264, 16
Pedregosa F. et al., 2011, J. Mach. Learn. Res., 12, 2825
Peñaloza C. H., Clark P. C., Glover S. C. O., Klessen R. S., 2018, MNRAS, 475, 1508
Peretto N., Lenfestey C., Fuller G. A., Traficante A., Molinari S., Thompson M. A., Ward-Thompson D., 2016, A&A, 590, A72
Perez F., Granger B. E., 2007, Comput. Sci. Eng., 9, 21
Planck Collaboration VI, 2020, A&A, 643, A42
Polychroni D., Moore T. J. T., Allsopp J., 2012, MNRAS, 422, 2992
Popescu C. C., Yang R., Tuffs R. J., Natale G., Rushton M., Aharonian F., 2017, MNRAS, 470, 2539
Querejeta M. et al., 2024, A&A, 687, A293
Ragan S. E., Moore T. J. T., Eden D. J., Hoare M. G., Elia D., Molinari S., 2016, MNRAS, 462, 3123
Rani R., Moore T. J. T., Eden D. J., Rigby A. J., 2022, MNRAS, 515, 271
Rani R., Moore T. J. T., Eden D. J., Rigby A. J., Duarte-Cabral A., Lee Y.-N., 2023, MNRAS, 523, 1832
Reid M. J. et al., 2019, ApJ, 885, 131
Rigby A. J. et al., 2016, MNRAS, 456, 2885
Rigby A. J. et al., 2019, A&A, 632, A58
Rosolowsky E. W., Pineda J. E., Kauffmann J., Goodman A. A., 2008, ApJ, 679, 1338
Sakamoto S., Hasegawa T., Handa T., Hayashi M., Oka T., 1997, ApJ, 486, 276
Schuller F. et al., 2009, A&A, 504, 415
Schuller F. et al., 2017, A&A, 601, A124
Sofue Y., Nakanishi H., 2016, PASJ, 68, 63
Su Y. et al., 2019, ApJS, 240, 9
Taylor M. B., 2005, in Shopbell P. L., Britton M. C., Ebert R., eds, ASP Conf. ser. Vol. 347, Astronomical Data Analysis Software and Systems XIV. Astron. Soc. Pac., San Francisco, p. 29
The Astropy Collaboration, 2022, ApJ, 935, 167
Umemoto T. et al., 2017, PASJ, 69
Urquhart J. S. et al., 2018, MNRAS, 473, 1059
Urquhart J. S. et al., 2021, MNRAS, 500, 3050
Urquhart J. S. et al., 2024, MNRAS, 528, 4746
Virtanen P. et al., 2020, Nat. Methods, 17, 261
Wienen M., Brunt C. M., Dobbs C. L., Colombo D., 2022, MNRAS, 509, 68
Wilson T. L., Rood R. T., 1994, ARA&A, 32, 191

APPENDIX A: ORAC-DR RECIPE PARAMETERS

In this Appendix, we list of several sections of the recipe parameters used for the data-reduction recipe REDUCE_SCIENCE_NARROWLINE in ORAC-DR. The first block relates to the pixel size and the binning method:

```
[REDUCE_SCIENCE_NARROWLINE]
#
# MAKECUBE parameters
PIXEL_SCALE  =  6.0
SPREAD_METHOD  =  Gauss
SPREAD_WIDTH  =  8
SPREAD_FWHM_OR_ZERO  =  6
#
REBIN  =  0.3
#
```

which specifies the use of 6.0-arcsec-wide pixels, and the use of a Gaussian smoothing kernel with FWHM of 8 arcsec to assist with the binning of pixel values onto the new pixel grid. The spreading function is curtailed at 6 arcsec, as specified by SPREAD_FWHM_OR_ZERO. Finally, the REBIN parameter specifies that the cube will be regridded to a 0.3 km s^{-1}-wide velocity channels.

```
# Tiling and chunking
TILE  =  0
CHUNKSIZE  =  12288
CUBE_MAXSIZE  =  1536
#
```

This block specifies that the entire cube should be treated as a single observation, and not be broken up into smaller tiles for memory-saving reasons. This produces a more convenient output.

```
# Baseline
BASELINE_ORDER  =  1
BASELINE_LINEARITY  =  1
BASELINE_LINEARITY_LINEWIDTH  =  -80:-20
```

The above parameters specify that a first-order polynomial baseline should be used for the fitting, and that the region of −80 to −20 km s^{-1} in the spectrum should be excluded when performing baseline linearity tests for each receptor.

```
# # Reference-spectrum removal from time-series cubes
#  --  Manual location
SUBTRACT_REF_SPECTRUM  =  1
REF_SPECTRUM_COMBINE_REFPOS  =  1
REF_SPECTRUM_REGIONS  =  -15.0:-11.5,14.0:17.0
```

This final set of parameters was optionally used in instances where off-position absorption was suspected to be present. This often reveals itself as a velocity range showing absorption features in the cube-average spectrum. By enabling SUBTRACT_REF_SPECTRUM and REF_SPECTRUM_COMBINE_REFPOS, ORAC-DR interpolates the reference spectrum across the velocity range or ranges identified in the REF_SPECTRUM_REGIONS setting, which consists of a comma-separated list of regions with suspected off-position emission. In this particular instance, the ranges of −15.0 to −11.5 and 14.0 to 17.0 km s^{-1} were interpolated over in the off- (reference-) position spectrum.

APPENDIX B: PREVIEW IMAGES OF THE PAMS REGIONS

In this appendix we display integrated intensity (moment 0) images of the PAMS regions in ^{12}CO, ^{13}CO, and C^{18}O(3–2), along with the corresponding position-velocity diagrams. We do not include NGC 7538 which has already been shown in Fig. 5. In all cases, the cubes have been masked using FELLWALKER, adopting the fwlores masks discussed in Section 3.3.

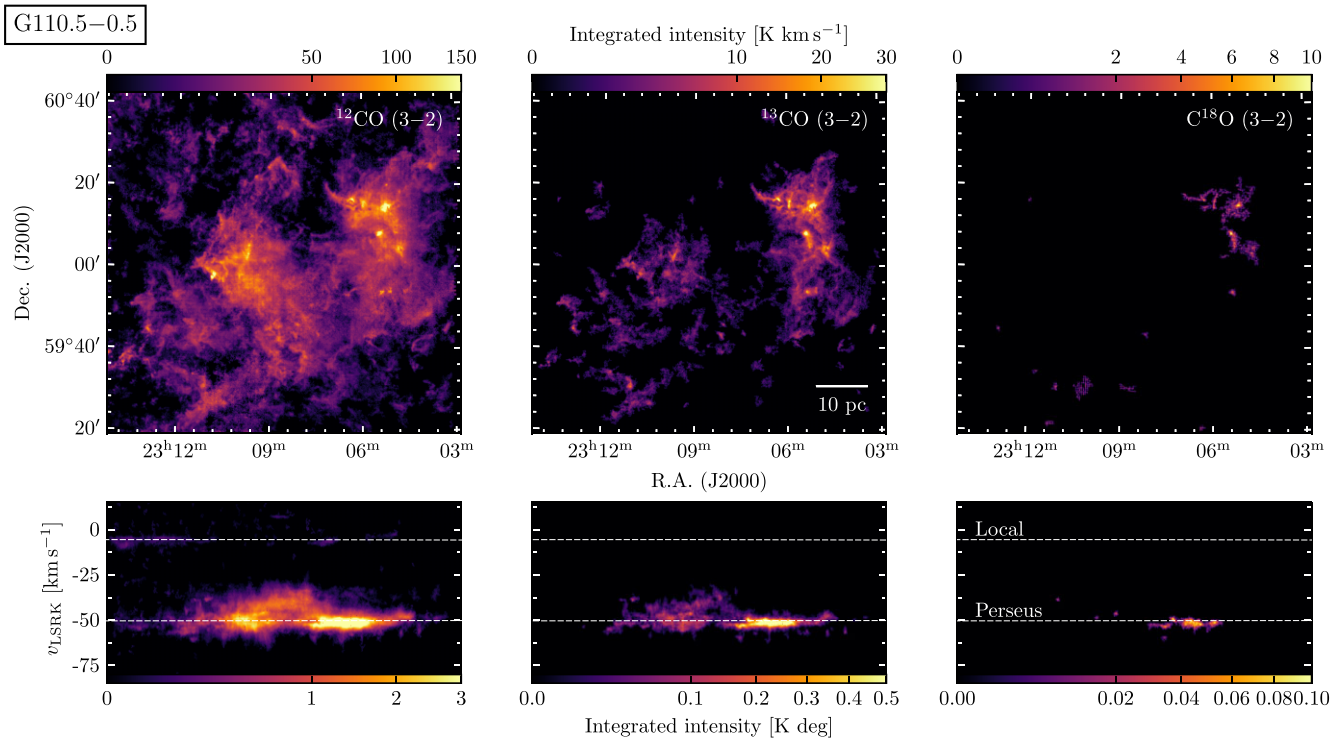

Figure B1. *Top row*: Integrated intensity (moment 0) maps of ^{12}CO, ^{13}CO, and C^{18}O (3–2) emission of G110.5+0.5. *Bottom row*: Position-velocity maps of the above maps integrated over declination.

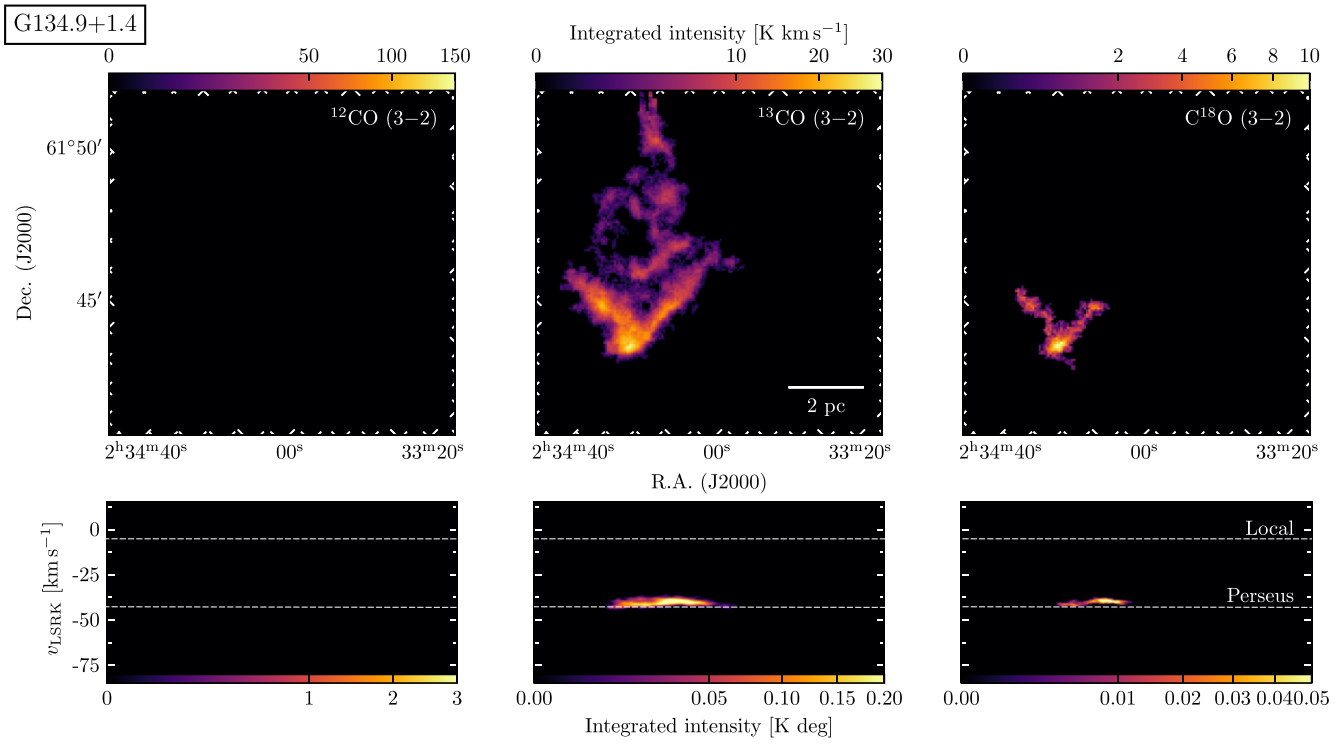

Figure B2. *Top row*: Integrated intensity (moment 0) maps of ^{12}CO, ^{13}CO, and C^{18}O (3–2) emission of G134.9+1.4. *Bottom row*: Position-velocity maps of the above maps integrated over the y-axis. There are no ^{12}CO (3–2) data for this region.

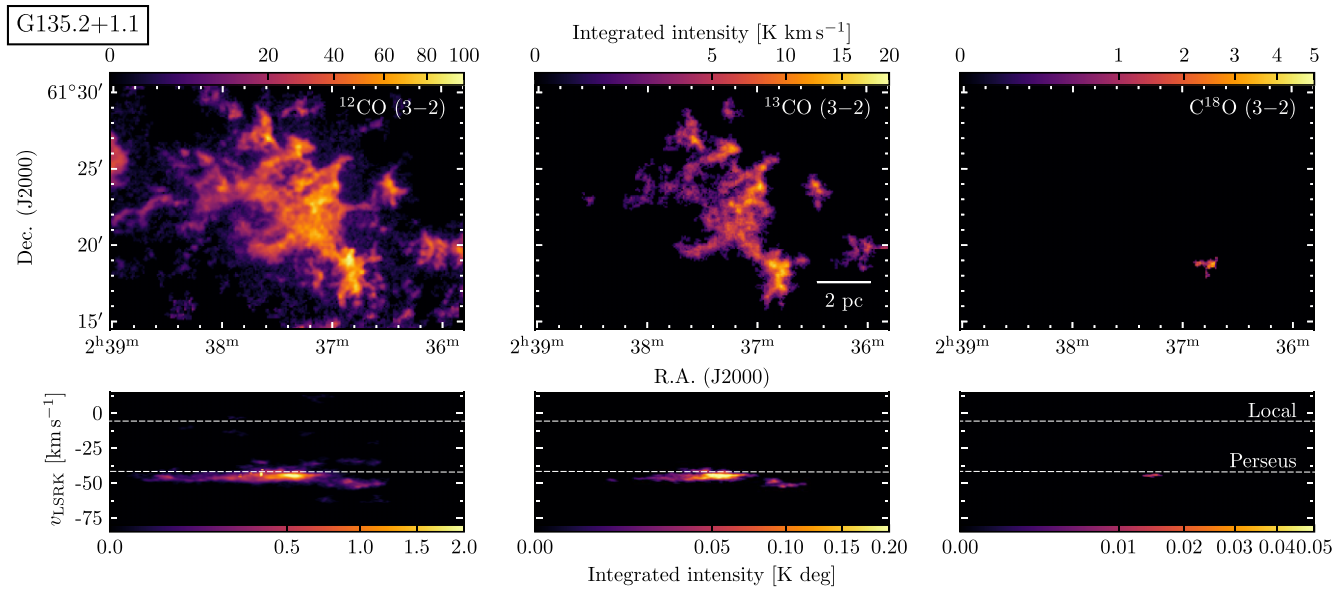

Figure B3. *Top row*: Integrated intensity (moment 0) maps of ^{13}CO, and C^{18}O (3–2) emission of G135.2+1.1. *Bottom row*: Position-velocity maps of the above maps integrated over declination.

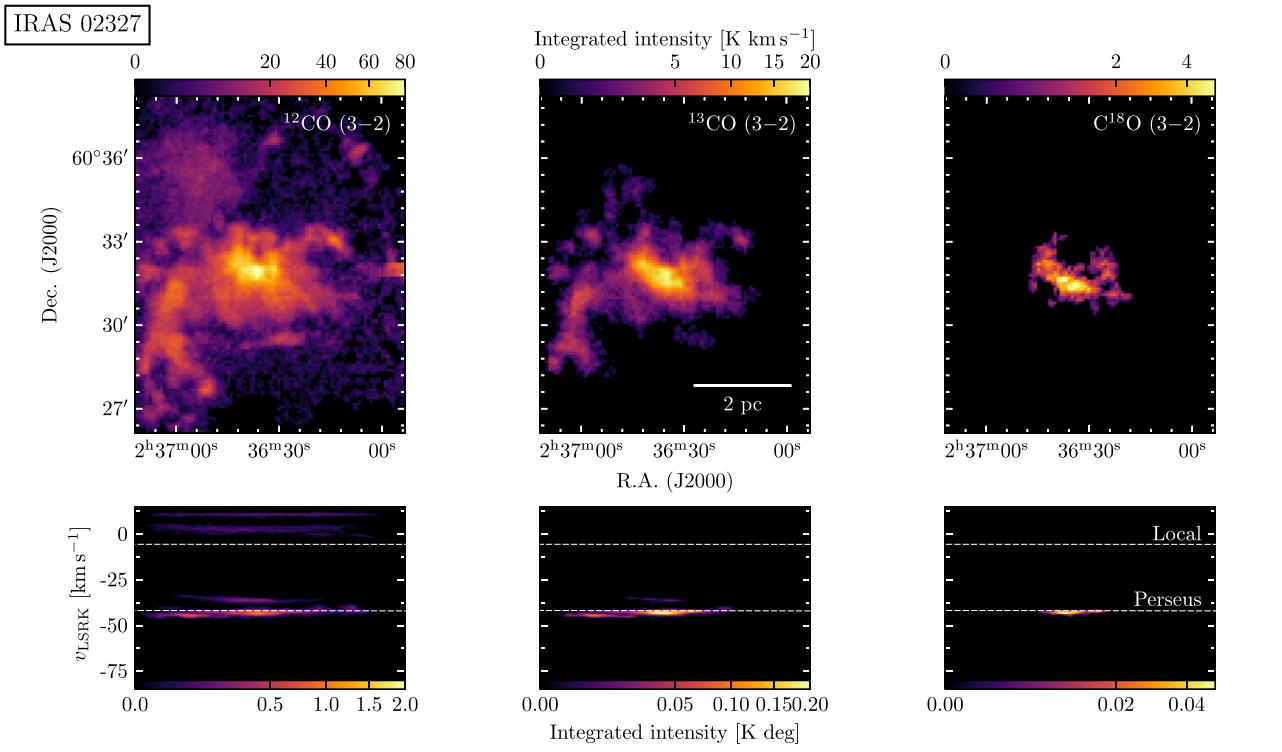

Figure B4. *Top row*: Integrated intensity (moment 0) maps of ^{12}CO, ^{13}CO, and C^{18}O (3–2) emission of G135.2+1.1. *Bottom row*: Position-velocity maps of the above maps integrated over declination.

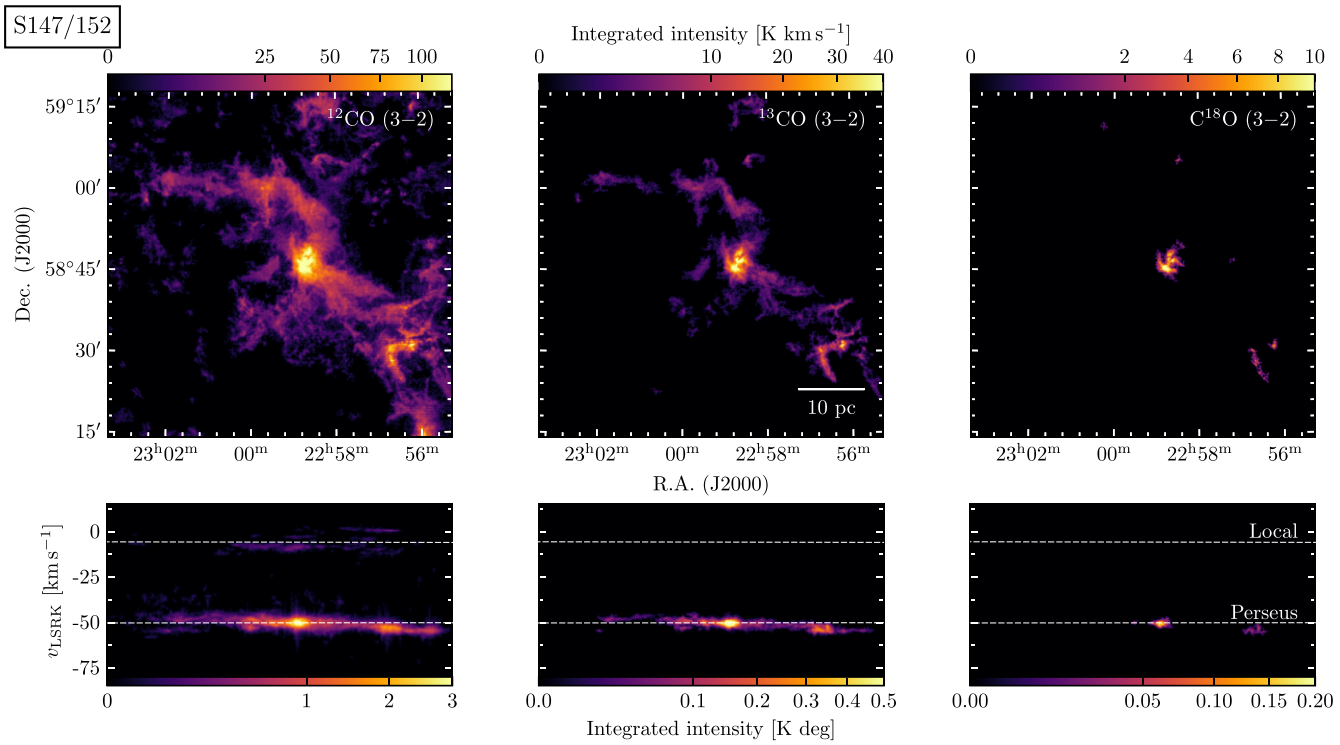

Figure B5. *Top row*: Integrated intensity (moment 0) maps of ^{12}CO, ^{13}CO, and C^{18}O (3–2) emission of S147/152. *Bottom row*: Position-velocity maps of the above maps integrated over declination.

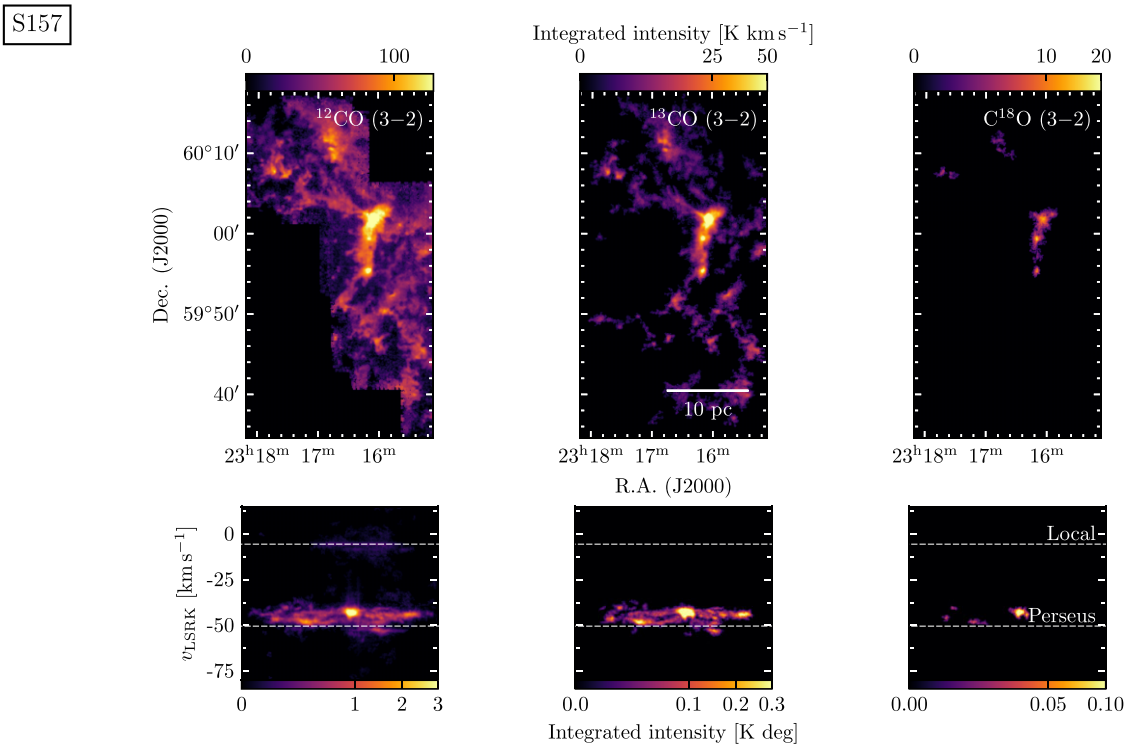

Figure B6. *Top row*: Integrated intensity (moment 0) maps of ^{12}CO, ^{13}CO, and C^{18}O (3–2) emission of S157. *Bottom row*: Position-velocity maps of the above maps integrated over declination.

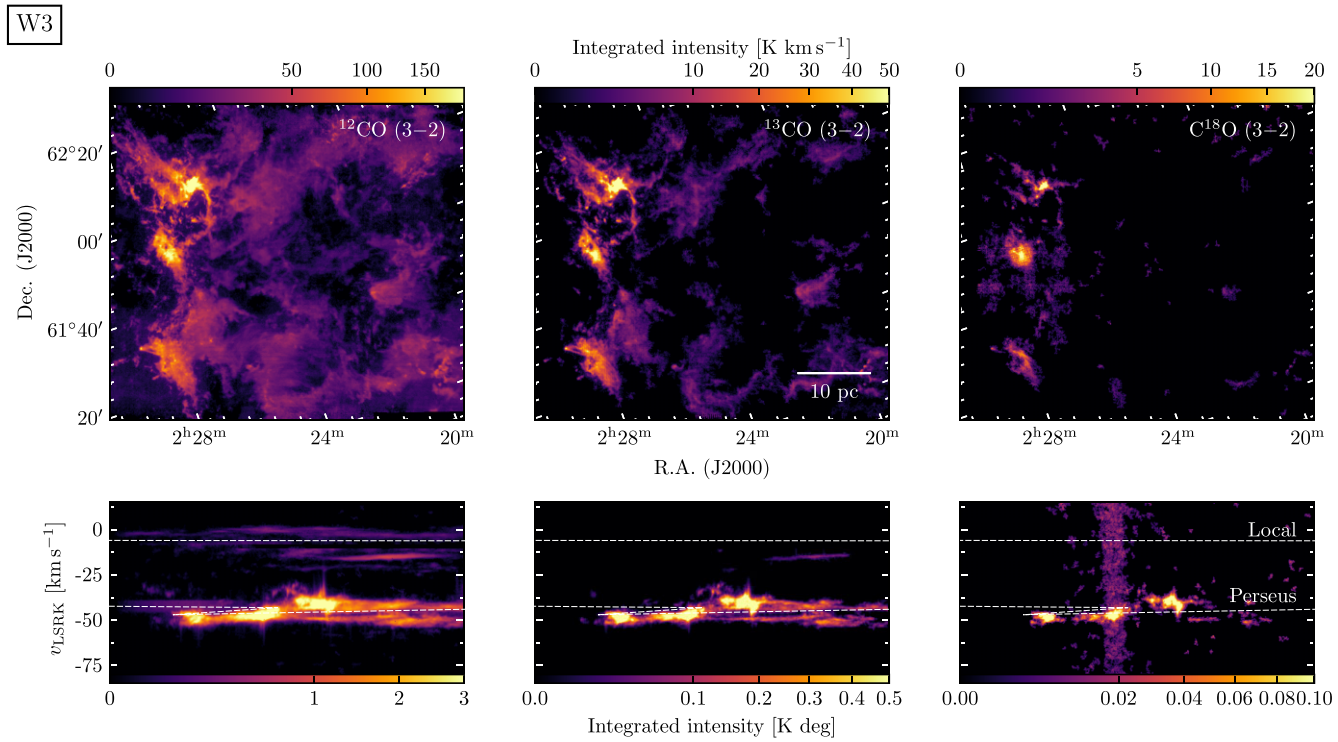

Figure B7. *Top row*: Integrated intensity (moment 0) maps of ^{12}CO, ^{13}CO, and C^{18}O (3–2) emission of W3. *Bottom row*: Position-velocity maps of the above maps integrated over the y-axis.

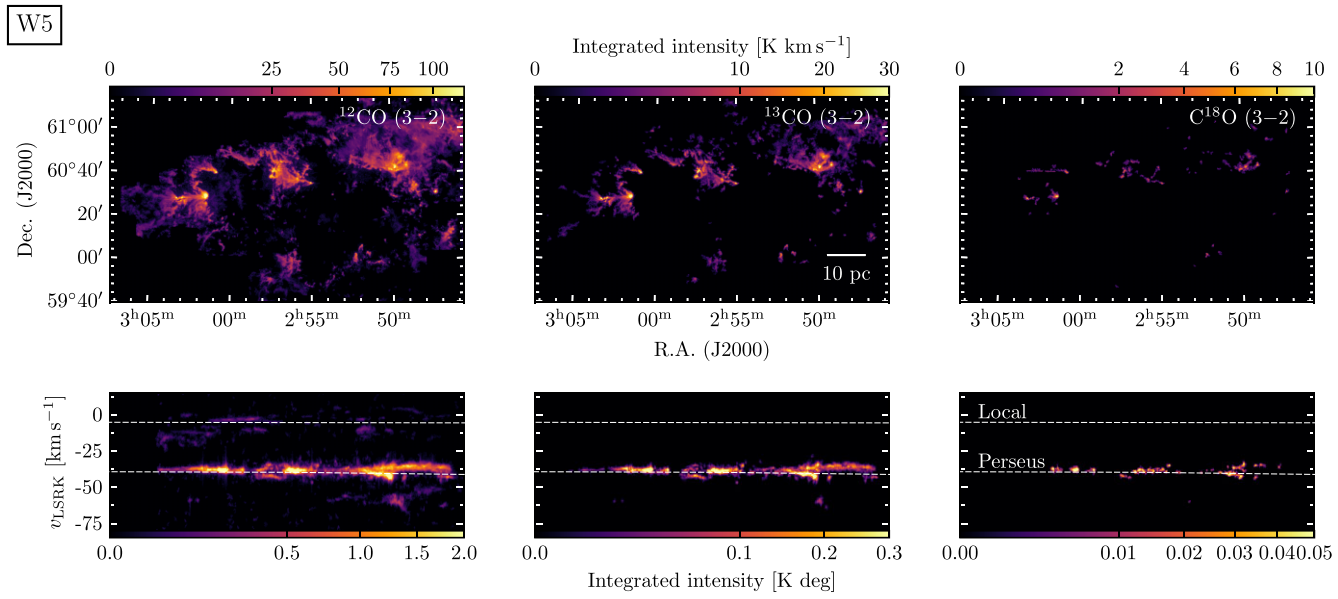

Figure B8. *Top row*: Integrated intensity (moment 0) maps of ^{12}CO, ^{13}CO, and C^{18}O (3–2) emission of W5. *Bottom row*: Position-velocity maps of the above maps integrated over the y-axis.

APPENDIX C: FELLWALKER CONFIGURATION

In Section 3.3 we described our usage of FELLWALKER to extract sources from the ^{13}CO (3–2) PAMS data. Our parameter setup for the `fwhires` extraction was as follows.

```
FellWalker.AllowEdge = 1
FellWalker.CleanIter = 0
FellWalker.FlatSlope = 1*RMS
FellWalker.FwhmBeam = 3
FellWalker.MaxBad = 0.05
FellWalker.MinDip = 5*RMS
FellWalker.MinHeight = 3*RMS
FellWalker.MinPix = 16
FellWalker.MaxJump = 0
```

```
FellWalker.Noise = 1*RMS
FellWalker.RMS = 1
FellWalker.VeloRes = 1
```

The parameter selection for the `fwlores` extraction was identical, with the following exception.

```
FellWalker.MinDip = 1000*RMS
```

This change effectively suppresses the ability of FELLWALKER to identify substructures within isolated islands of emission, and thus will recover the largest possible complexes of contiguous pixels of emission.

The parameters used for the `fwchimps` extraction were the same as for `fwhires` with the following alterations.

```
FellWalker.AllowEdge = 0
FellWalker.CleanIter = 1
FellWalker.MaxJump = 4
FellWalker.RMS = 1.7
FellWalker.VeloRes = 0
```

This setup was chosen to match the extraction of Rigby et al. (2016) as closely as possible. The key difference is that `RMS` is set to 1.7 to reflect higher noise levels in the CHIMPS compared with PAMS data after smoothing to 27.4-arcsec resolution. The parameters `FlatSlope`, `MinDip`, `MinHeight`, and `Noise` are scaled up by the same amount. The differences between the `fwhires` setup compared with `fwchimps` were generally selected to combat spurious sources, and especially the archipelago source types discussed briefly in Section 4.2; setting both `CleanIter` and `MaxJump` to zero, and `VeloRes` to 1 helps suppress these source types. It was also necessary to adopt value of 1 for `AllowEdge` due to the extra sensitivity and targeted mapping of the PAMS observations, which meant that emission was often detected up to the edges of the image, and a zero value would have excluded significant sources.

APPENDIX D: FELLWALKER CATALOGUE DESCRIPTIONS

The columns featuring in the `fwhires`, `fwlores`, and `fwchimps` catalogues are listed Table D1. The only difference between the three is that the `fwhires` catalogue features an additional `Parent_ID` column, which allows the `fwhires` sources to be connected to their parent larger scale structure in the `fwlores` extraction.

Table D1. Column descriptions for the provided catalogues.

Column number	Name	Data type	Units	Description
1	Region	string	None	PAMS region
2	ID	integer	None	Voxel ID in mask
3	RA_cen	float	deg	Centroid RA coordinate
4	Dec_cen	float	deg	Centroid Dec coordinate
5	Vlsr_cen	float	km s^{-1}	Centroid $v_{\rm LSR}$ coordinate
6	RA_peak	float	deg	Peak RA coordinate
7	Dec_peak	float	deg	Peak Dec coordinate
8	Vlsr_peak	float	km s^{-1}	Peak $v_{\rm LSR}$ coordinate
9	Sigma_RA	float	arcsec	Intensity-weighted dispersion in RA
10	Sigma_Dec	float	arcsec	Intensity-weighted dispersion in Dec
11	Sigma_Vlsr	float	km s^{-1}	Intensity-weighted dispersion in $v_{\rm LSR}$
12	Sigma_Vlsr_corrected	float	km s^{-1}	Estimated linewidth corrected for SNR
13	Sigma_Vlsr_err	float	km s^{-1}	Uncertainty on linewidth
14	Sum	float	K	Sum of ^{13}CO (3–2) voxel values
15	Peak	float	K	Peak ^{13}CO (3–2) voxel value
16	major_sigma	float	deg	Semi-major axis of ellipse
17	minor_sigma	float	deg	Semi-minor axis of ellipse
18	position_angle	float	deg	Position angle of ellipse (E of N)
19	n_pixels	integer	None	Number of pixels in projected area
20	n_voxels	integer	None	Number of voxels in source
21	polygon	string	None	(RA, Dec) vertices of polygon describing source
22	RA_cen_snr	float	deg	Centroid RA coordinate in SNR cube
23	Dec_cen_snr	float	deg	Centroid Dec coordinate in SNR cube
24	Vlsr_cen_snr	float	km s^{-1}	Centroid $v_{\rm LSR}$ coordinate in SNR cube
25	RA_peak_snr	float	deg	Peak RA coordinate in SNR cube
26	Dec_peak_snr	float	deg	Peak Dec coordinate in SNR cube
27	Vlsr_peak_snr	float	km s^{-1}	Peak $v_{\rm LSR}$ coordinate in SNR cube
28	Sigma_RA_snr	float	arcsec	Intensity-weighted dispersion in RA in SNR cube
29	Sigma_Dec_snr	float	arcsec	Intensity-weighted dispersion in Dec in SNR cube
30	Sigma_Vlsr_snr	float	km s^{-1}	Intensity-weighted dispersion of $v_{\rm LSR}$ in SNR cube
31	Sum_snr	float	None	Sum of voxel values in SNR cube
32	Peak_snr	float	None	Peak voxel value in SNR cube
33	dkpc	float	kpc	Heliocentric distance to region
34	derr	float	kpc	Error on heliocentric distance to region
35	Rgc	float	kpc	Galactocentric radius of region
36	R_eq_arcsec_nodec	float	arcsec	Radius of circle with equivalent area
37	R_eq_arcsec	float	arcsec	Beam-deconvolved radius of circle with equivalent area
38	R_eq_pc	float	pc	Beam-deconvolved radius of circle with equivalent area
39	R_eq_pc_err	float	pc	Error on R_eq_pc
40	R_sig_arcsec_nodec	float	arcsec	Intensity-weighted radius
41	R_sig_arcsec	float	arcsec	Beam-deconvolved intensity-weighted radius
42	R_sig_pc	float	pc	Beam-deconvolved intensity-weighted radius
43	R_sig_pc_err	float	pc	Error on R_sig_pc
44	Mass_Xco	float	$M_\odot$	Mass estimated using ^{13}CO (3–2) X-factor
45	Mass_Xco_lo	float	$M_\odot$	16th percentile of Mass_Xco distribution
46	Mass_Xco_up	float	$M_\odot$	84th percentile of Mass_Xco distribution
47∗	Parent_ID	integer	None	ID of parent source in fwlores catalogue

∗ (fwhires catalogue only).

This paper has been typeset from a TEX/LATEX file prepared by the author.